Supplementary Information

Giant energy storage density with ultrahigh efficiency in multilayer ceramic capacitors via interlaminar strain engineering

Ying Yang[1,#], Ke Xu[2,#], Bin Yang[3,#], Xu Hou[4], Zhanming Dou[1], Yuhong Li[1], Zihao Zheng[3], Gengguang Luo[1,5], Nengneng Luo[5], Guanglong Ge[6], Jiwei Zhai[6], Yuanyuan Fan[2], Jing Wang[2], Haoming Yang[7], Yao Zhang[7], Jing Wang[8], Changyuan Wang[1], Shenglin Jiang[1], Kanghua Li[1,*], Jinming Guo[3,*], Houbing Huang[2,*] and Guangzu Zhang[1,*]

[1]School of Integrated Circuits, Huazhong University of Science and Technology, Wuhan, China. [2]Advanced Research Institute of Multidisciplinary Science, and School of Materials Science & Engineering, Beijing Institute of Technology, Beijing, China. [3]Electron Microscopy Center, Ministry-of-Education Key Laboratory of Green Preparation and Application for Functional Materials, School of Materials Science and Engineering, Hubei University, Wuhan, China. [4]Department of Industrial and Systems Engineering, Research Institute for Advanced Manufacturing, The Hong Kong Polytechnic University, Hung Hom, Kowloon, Hong Kong, China. [5]State Key Laboratory of Featured Metal Materials and Life-cycle Safety for Composite Structures, School of Resources, Environment and Materials, Guangxi University, Nanning, China. [6]Shanghai Key Laboratory for R&D and Application of Metallic Functional Materials, Functional Materials Research Laboratory, School of Materials Science and Engineering, Tongji University, Shanghai, China. [7]Department of Engineering Mechanics, School of Aerospace Engineering, Huazhong University of Science and Technology, Wuhan, China. [8]College of Chemistry and Materials Science, Hebei University, Baoding, China. [#]These authors contributed equally: Ying Yang, Ke Xu, Bin Yang. email: kanghua_li@hust.edu.cn; guojinming@hubu.edu.cn; hbhuang@bit.edu.cn; zhanggz@hust.edu.cn

Contents

Note S1. Heat generation in MLCCs.

In multilayer ceramic capacitors, heat generated during the charge-discharge process originates mainly from dielectric losses (i.e., polarization hysteresis loss and leakage loss)[1]. According to the energy conservation law, the rate of heat storage determined by the heat generation and dissipation effects can be expressed as[2]:

$$\dot{q}_{\mathrm{G}} - \dot{q}_{\mathrm{out}} = \rho v c \frac{\mathrm{d}T}{\mathrm{d}t} \tag{1}$$

where $\dot{q}_{\mathrm{G}}$ and $\dot{q}_{\mathrm{out}}$ are the heat generation and dispassion rates, respectively, ρ is the density, c is the specific heat, and v is the volume of the dielectric material. The heat generation rate $\dot{q}_{\mathrm{G}}$ can be expressed as[2]:

$$\dot{q}_{\mathrm{G}} = u f v_{\mathrm{e}} \tag{2}$$

where u is the hysteresis loss per unit volume per driving cycle, f is the driving frequency, and v_{e} is the effective volume (the dielectric material covered with electrodes). The heat dissipation rate $\dot{q}_{\mathrm{out}}$ is the sum of the radiation heat transfer rate $\dot{q}_{\mathrm{r}}$ and the convection heat transfer rate $\dot{q}_{\mathrm{c}}$ [Ref. 2]:

$$\dot{q}_{\mathrm{out}} = \dot{q}_{\mathrm{r}} + \dot{q}_{\mathrm{c}} \tag{3}$$

According to the Stefan-Boltzmann radiation law[3]:

$$\dot{q}_{\mathrm{r}} = \sigma \varepsilon A\left(T^4 - T_0^4\right) \tag{4}$$

where σ is the Stefan-Boltzmann constant [5.67×10^{-8} W/(m^{2}K^4)], ε is the emissivity of the material and A is the total surface area of the sample. T is the temperature of the material and T_0 is the temperature of the fluid or gas surrounding the material surface. According to the Newton's law of cooling[3]:

$$\dot{q}_{\mathrm{c}} = \bar{h} A (T - T_0) \tag{5}$$

where $\bar{h}$ is the average convective heat transfer coefficient. Thus, $\dot{q}_{\mathrm{out}}$ can be expressed as:

$$\dot{q}_{\mathrm{out}} = \sigma \varepsilon A\left(T^4 - T_0^4\right) + \bar{h} A (T - T_0) \tag{6}$$

Hence,

$$\dot{q}_{\mathrm{G}} - \dot{q}_{\mathrm{out}} = ufv_{\mathrm{e}} - A\left[\sigma\varepsilon\left(T^4 - T_0^4\right) + \bar{h}(T - T_0)\right] = \rho vc\frac{\mathrm{d}T}{\mathrm{d}t} \tag{7}$$

Equation (7) can be written as:

$$ufv_{\mathrm{e}} - Ak(T)(T - T_0) = \rho vc\frac{\mathrm{d}T}{\mathrm{d}t} \tag{8}$$

$$k(T) = \sigma\varepsilon\left(T^2 + T_0^2\right)(T + T_0) + \bar{h} \tag{9}$$

where $k(T)$ is the overall heat transfer coefficient. Finally, the temperature rise (ΔT) as a function of time (t) can be calculated as:

$$\Delta T = T - T_0 = \frac{ufv_{\mathrm{e}}}{k(T)A}\left(1 - \mathrm{e}^{-\left(\frac{k(T)A}{v\rho c}\right)t}\right) \tag{10}$$

As $t \to \infty$,

$$\Delta T = \frac{fv_{\mathrm{e}}}{k(T)A}u \tag{11}$$

Note S2. The reasons for choosing lead-based antiferroelectrics for the research.

Compared with linear dielectrics, nonlinear dielectrics including ferroelectric (FE) and antiferroelectric (AFE) materials have higher polarization, endowing them with much higher energy storage density. Moreover, due to the double hysteresis loops, AFEs always have lower remanent polarization and superior energy efficiency in comparison to that of FEs. Besides, AFEs possess a large electrostriction effect that enables the polarization behavior and the energy storage performance of the MLCCs to be manipulated via strain engineering. Thus, in this work, we investigated the energy storage feature of MLCCs with AFE dielectrics.

Although strenuous efforts have been dedicated to improving the properties (e.g., dielectric, piezoelectric, pyroelectric and electrostriction properties) of lead-free FE and AFE ceramics in the last twenty years, the performances of the lead-free materials, especially AFE ceramics, are still inferior to that of lead-based compositions. Taking two typical lead-free AFE ceramics, $AgNbO_3$ and $NaNbO_3$, for example, $AgNbO_3$ possesses high polarization close to that of lead-based AFE materials such as $(Pb_{0.94}La_{0.04})(Zr_{0.99}Ti_{0.01})O_3$ and $Pb_{0.97}La_{0.02}(Zr_{0.93}Sn_{0.05}Ti_{0.02})O_3$[4-6], however, the remanent polarization of $AgNbO_3$ is also high, which can be ascribed to its orthorhombic (*Pmc*21) lattice structure with uncompensated ion displacement (FIE phase) that is distinct from the typical the centrosymmetric *Pbcm* structure (AFE phase)[7]. Even though the remanent polarization of $AgNbO_3$ can be depressed with elements doping, e.g., La ions, the remanent polarization is still significantly higher than that of $(Pb_{0.98}La_{0.02})(Zr_{0.55}Sn_{0.45})_{0.995}O_3$[8,9]. For $NaNbO_3$, owing to the minute difference between the free energy barriers of AFE and field-induced FE phases, the AFE and FE phases are in a metastable state, making the typical AFE double hysteresis loops unobvious. Although the AFE phase could be stabilized with composition designs[10,11], the hysteresis of $NaNbO_3$ is large, which means the energy consumed for the

AFE-FE phase transition is high, resulting in an unfavorable energy storage efficiency[12-14].

Different from the lead-free antiferroelectrics, a stable AFE phase could be obtained in $PbZrO_3$ with La^{3+}, Sn^{4+}, and Ti^{4+} doping. In addition, the polarization behavior and the electrostriction effect of the $PbZrO_3$-based materials can be tuned by composition design effectively. As we demonstrated, $(Pb_{0.95}Ba_{0.02}La_{0.02})(Zr_{0.6}Sn_{0.4})O_3$ (PBLZS) possesses high polarization and electric field-induced strain, while $(Pb_{0.9}Ba_{0.04}La_{0.04})(Zr_{0.65}Sn_{0.3}Ti_{0.05})O_3$ (PBLZST) and $(Pb_{0.92}Ca_{0.06}La_{0.02})(Zr_{0.6}Sn_{0.4})_{0.995}O_3$ (PCLZS) possess near-zero remanent polarization. Furthermore, even with different polarization and electrostriction characteristics, the sintering temperature, e.g., the temperature for the stimulation of the solid-state mass transfer of most lead-based AFE ceramics are similar, matching the fabrication process requirement for MLCCs well. Thus, we fabricated MLCCs with lead-based antiferroelectric materials and explored their energy storage potential with the interlaminar strain engineering strategy.

It is believed that with further efforts, breakthroughs could be achieved in lead-free FE and AFE ceramics. We thus anticipate expanding the strain engineering strategy available to lead-free AFE MLCCs for high energy storage performance in the future.

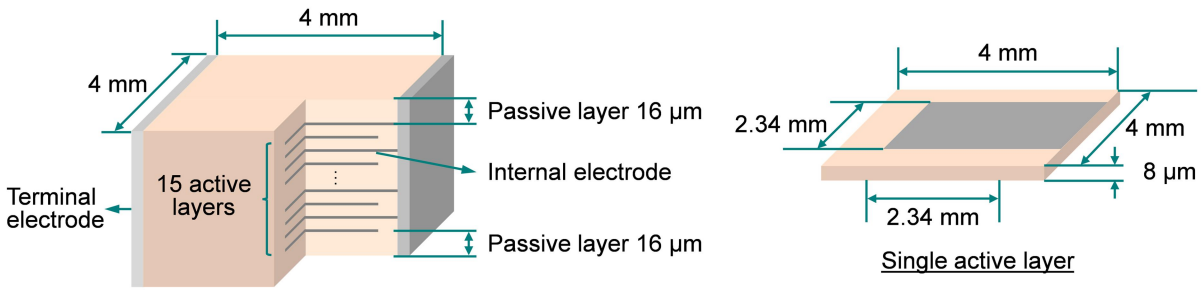

Fig. S1 | Dimension of the sintered MLCCs. The dimensions of the sintered MLCCs are: length L=4 mm, width W=4 mm, thickness T=0.17 mm (including the passive layers). Each MLCC consists of 15 active layers (thickness of ~8 μm) and 2 sacrificial layers (top and bottom passive layers with thickness of ~16 μm). The printed electrode area is 3 mm×3 mm (overlap part). Taking the shrinkage rate of 22% during the sintering process into consideration, the effective electrode area is 3 mm×3 mm×(1-22%)=5.48 mm^2. The total thickness of the active layers is 8 μm×15 layers=120 μm, which is much larger than that of the top and bottom passive layers (32 μm), and thus it is believed the influence of the passive layers on the stress engineering is limited. The active part of the MLCC has a volume of 5.48 mm^2×8 μm (thickness of single layer)×15 layers=0.66 mm^3, and the passive part has a volume of 4 mm×4 mm×0.17 mm−0.66 mm^3 = 2.06 mm^3. Thus, the ratio of the active part to the passive part of the MLCCs is 0.66 mm^3 : 2.06 mm^3≈1 : 3.12.

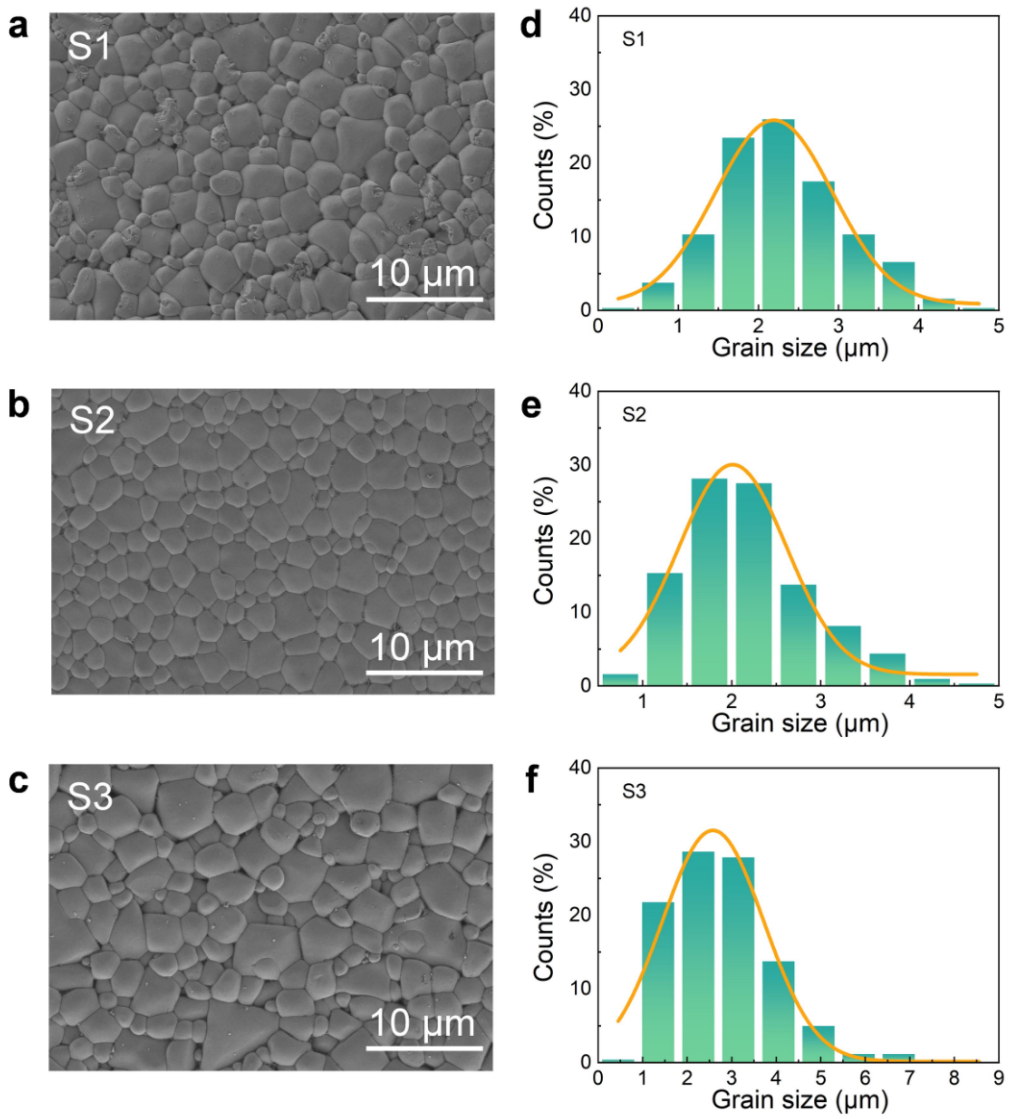

Fig. S2 | The SEM surface morphology and grain size distribution of the samples. a-c Surface SEM images of S1, S2, and S3. **d-f** Grain size distribution of S1, S2, and S3. The average grain sizes of S1, S2, and S3 are 2.3 μm, 2.2 μm, and 2.8 μm, respectively.

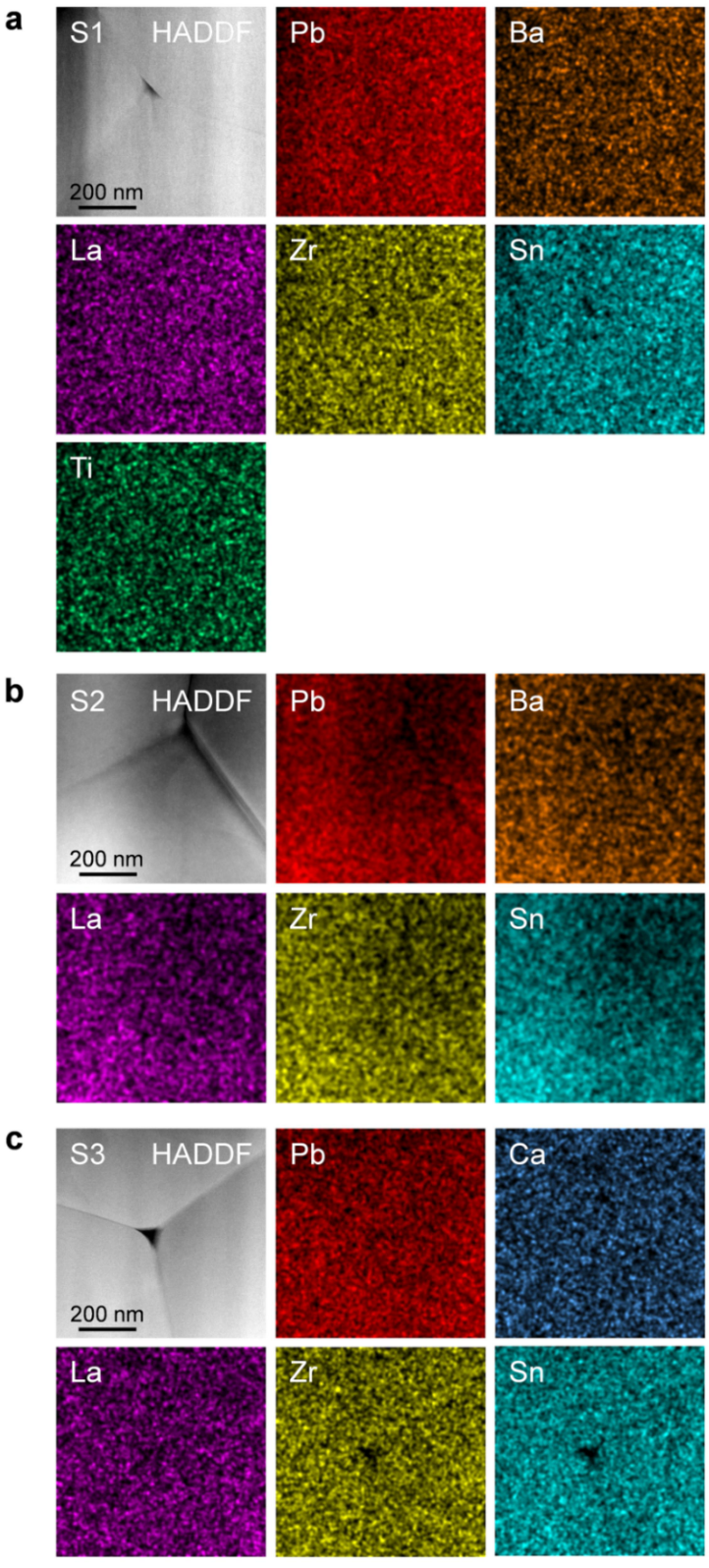

Fig. S3 | Submicrometer-scale EDS mapping. HAADF-STEM images and the corresponding EDS elemental mappings of **a** S1, **b** S2, and **c** S3.

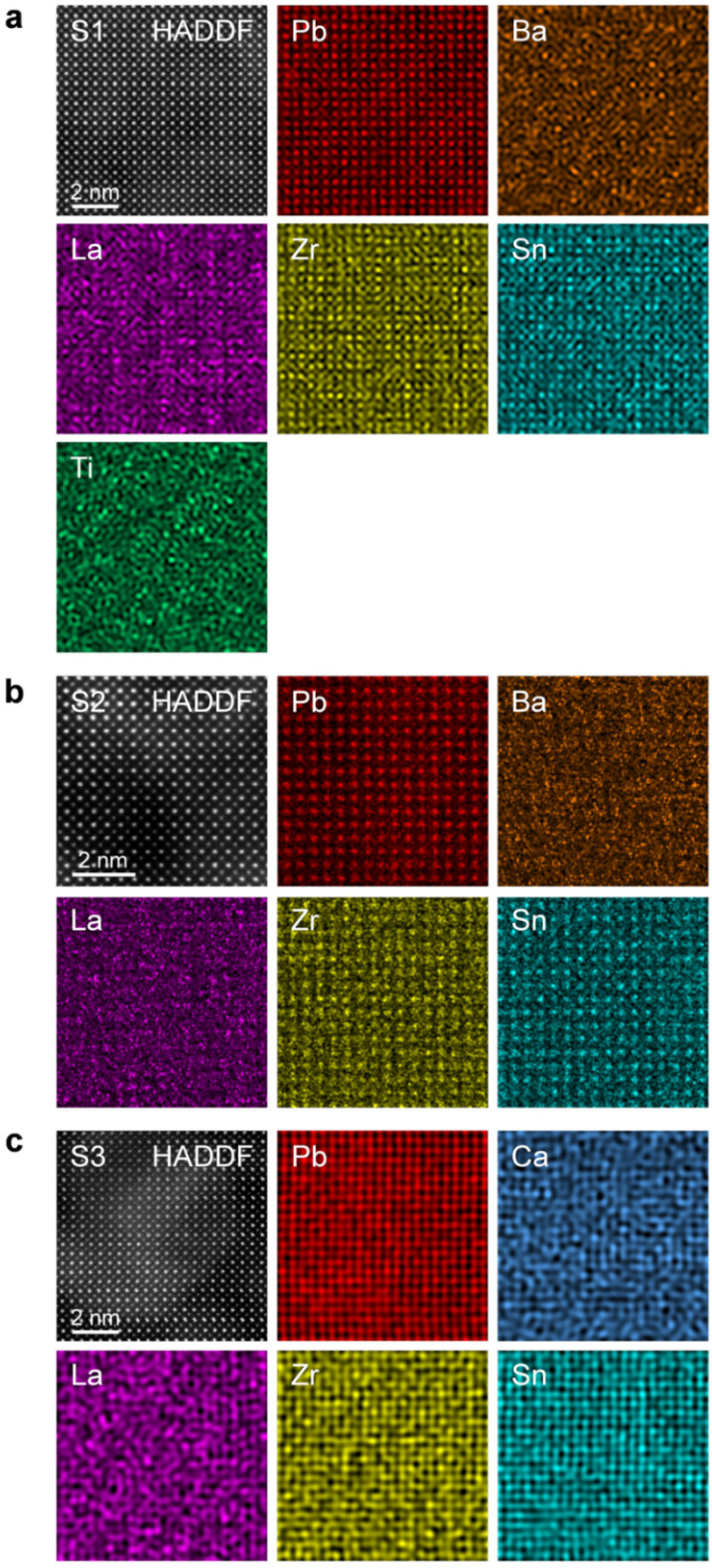

Fig. S4 | Atomic-scale EDS mapping. HAADF-STEM images and the corresponding atomic-resolution EDS elemental mappings of **a** S1, **b** S2, and **c** S3 along the [100] zone axes.

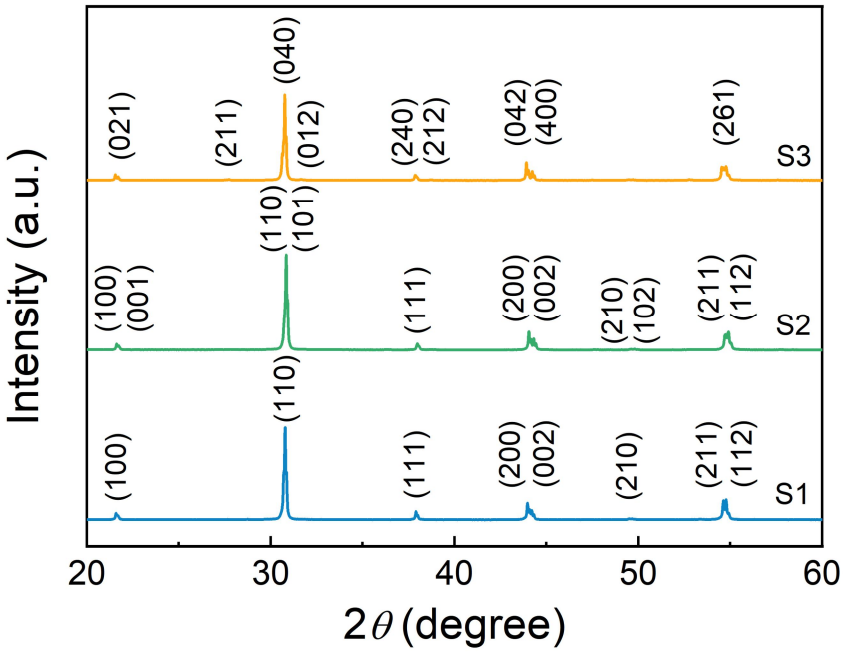

Fig. S5 | XRD patterns of S1, S2, and S3.

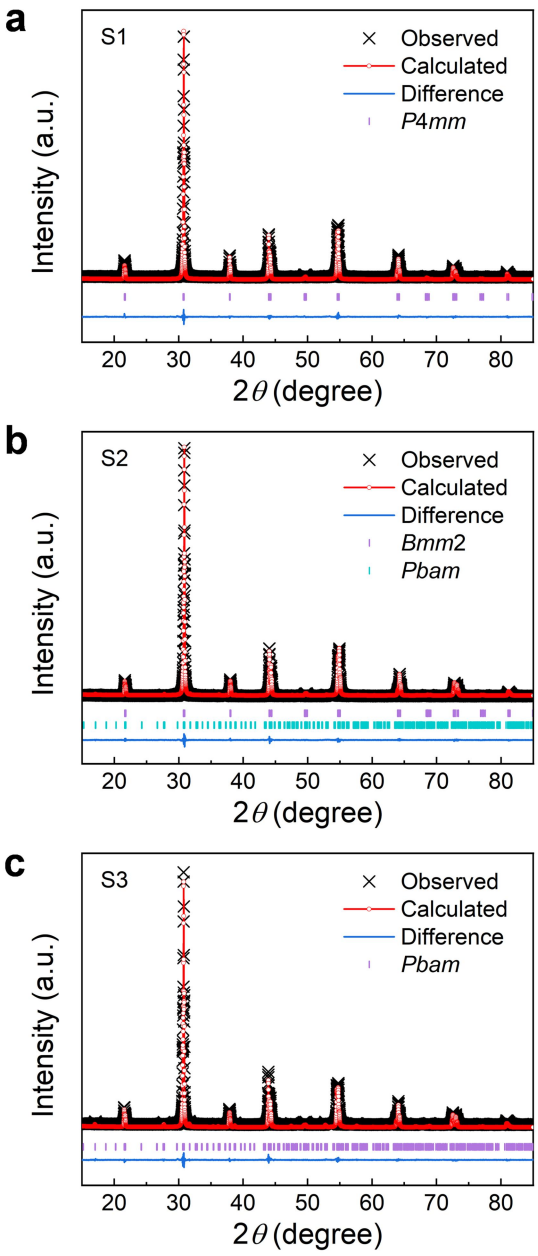

Fig. S6 | XRD refinement results. a XRD refinement result of S1. S1 exhibits a tetragonal phase with the *P*4*mm* space group. **b** XRD refinement result of S2. S2 consists of two phases: the O_I phase with an orthorhombic structure in the *Pbam* space group, and the O_{II} phase with the *Bmm*2 space group. **c** XRD refinement result of S3. S3 is identified to be the orthorhombic phase with the *Pbam* space group.

Note of Fig. S6.

The XRD patterns were refined with the Rietveld method by using the Generalized Structure and Analysis Software (GSAS)[15], and the results are exhibited in Fig. S6, where the observed and fitted curves are represented by "×" and red solid line, respectively. The difference in the intensity between the observed and fitted data is represented by the blue solid line, and the small difference indicates that the refined structural parameters are in good agreement with the actual diffraction pattern of the samples. This difference can be evaluated using the reliability factors of patterns (R_p) and the goodness-of-fit indicator (χ^2). Specifically, the refinement is regarded as reliable when R_p and χ^2 are in the reasonable ranges of 5.56%-6.39% and 1.249-1.455, respectively[16]. The R_p and χ^2 listed in Table S2 demonstrate the high reliability of our refinement. The purple vertical lines represent the theoretically calculated diffraction angle positions (i.e., allowed peak positions) based on Bragg's law, reflecting the crystal symmetry and space group of the materials. With the refinement, the lattice parameters of S1-S3 are listed in Table S2. The results revealed that S1 and S3 have the pure tetragonal phase belonging to the *P*4*mm* space group and the orthorhombic phase of the *Pbam* space group, respectively, while S2 is composed of two orthorhombic phases, e.g., 80.8% O_I phase belonging to the *Pbam* space group and 19.2% O_{II} phase of the *Bmm*2 space group.

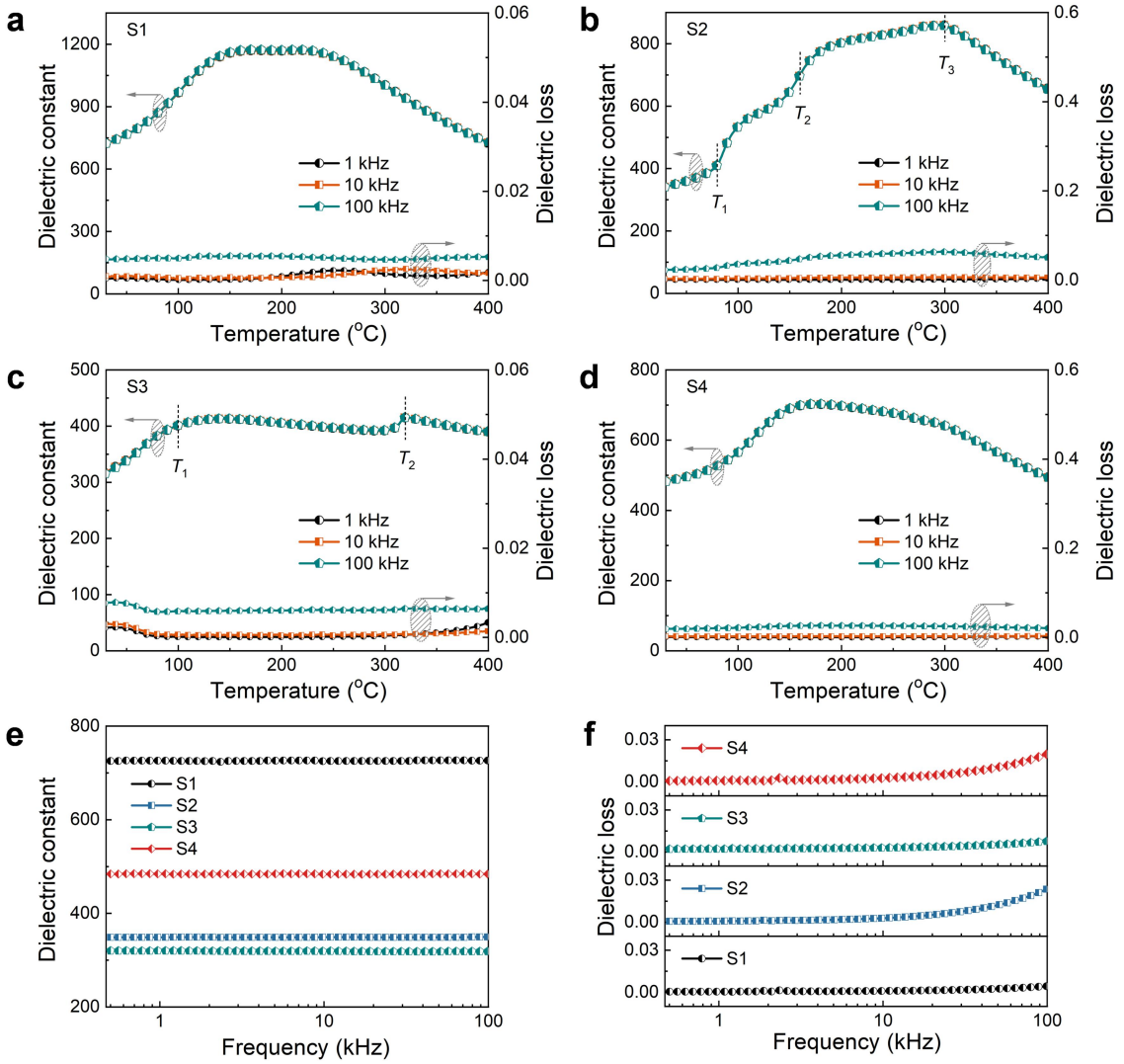

Fig. S7 | Dielectric constant and loss of S1-S4 MLCCs. Temperature-dependent dielectric constant and loss of **a** S1, **b** S2, **c** S3, and **d** S4 MLCCs. **e**,**f** Frequency-dependent dielectric constant and loss of S1-S4 MLCCs at room temperature.

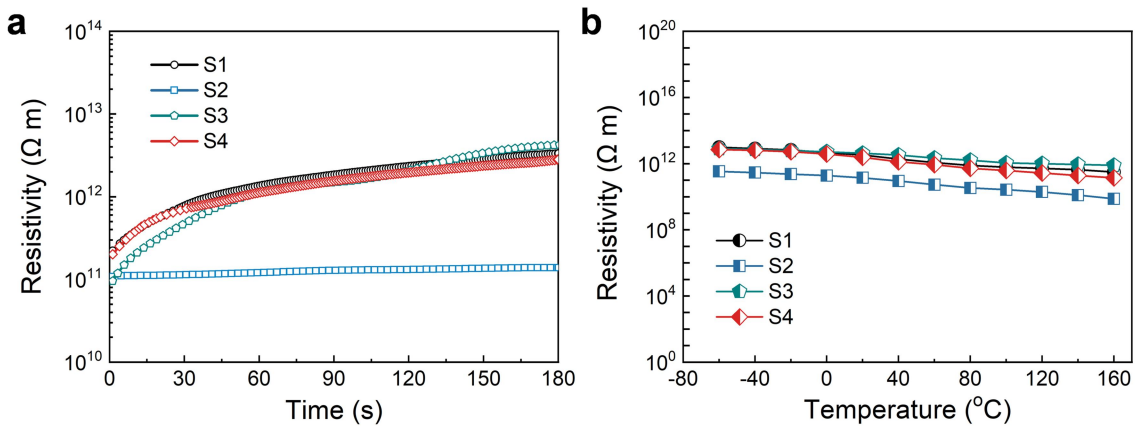

Fig. S8 | Electric resistivity of S1-S4 MLCCs. a Resistivity of S1-S4 MLCCs at room temperature with an electric field of 100 kV cm^{-1}. **b** Resistivity of S1-S4 MLCCs at different temperatures with an electric field of 100 kV cm^{-1}.

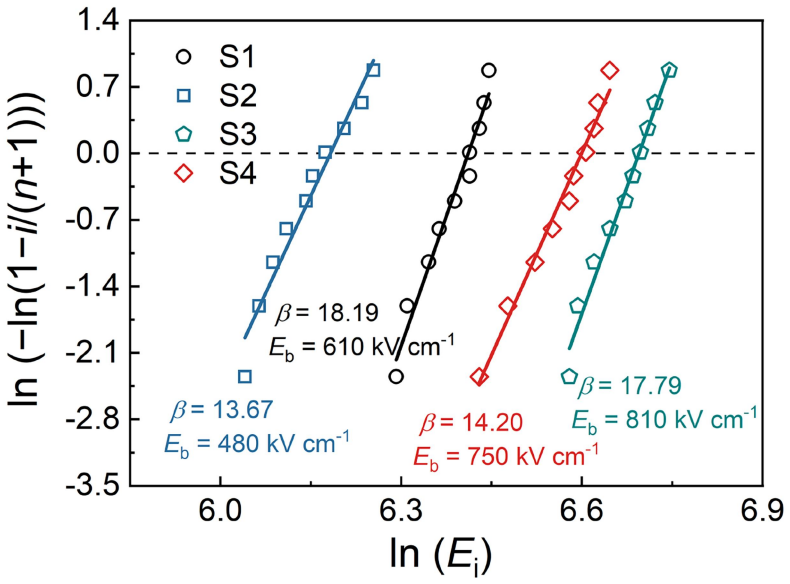

Fig. S9 | Weibull distribution analysis of breakdown strength of S1-S4 MLCCs. The shape factor (β) of the Weibull distribution is larger than 10, demonstrating that the experimental data possesses high reliability[17,18]. E_b is extracted from the points where the fitting lines intersect with the horizontal line through $\ln(-\ln(1 - i/(n + 1))) = 0$ (where i is the serial number of samples and n is the sum of samples). E_b of S1, S2, S3 and S4 are 610 kV cm^{-1}, 480 kV cm^{-1}, 810 kV cm^{-1} and 750 kV cm^{-1}, respectively.

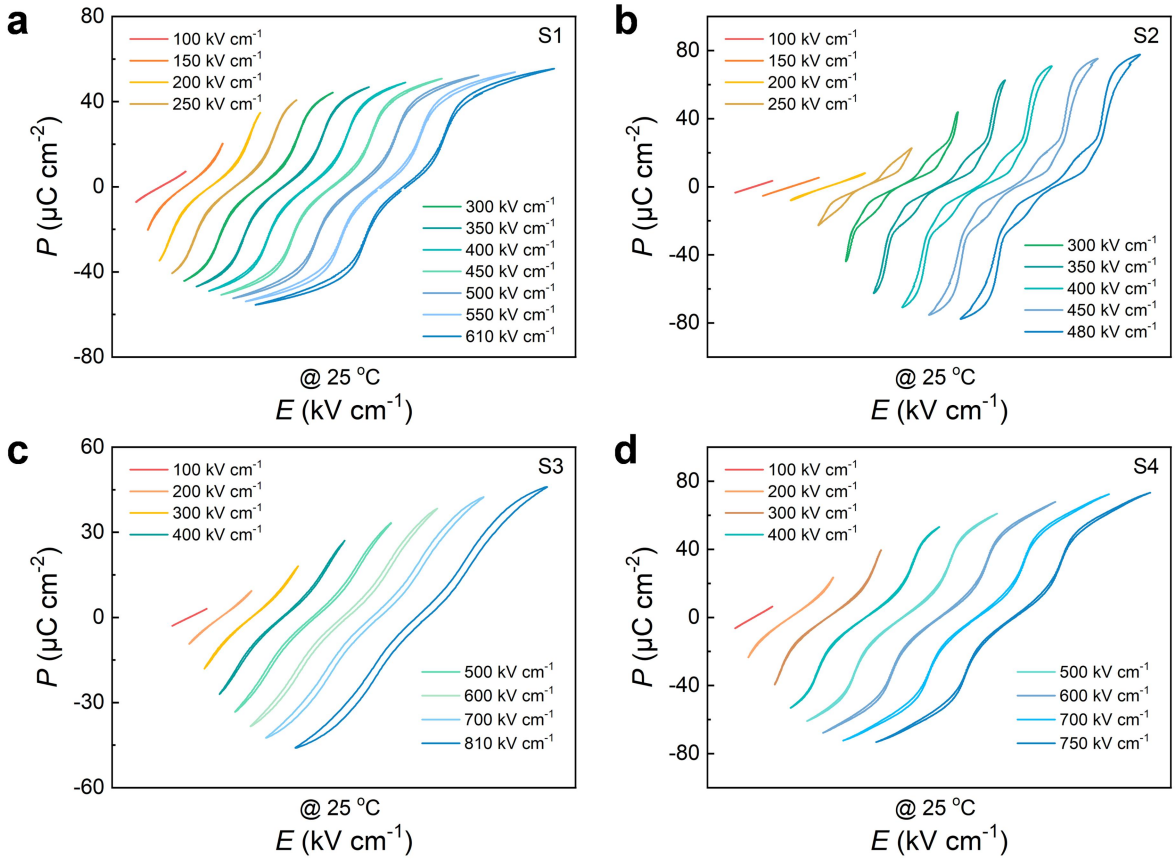

Fig. S10 | *P-E* loops measured at different electric fields. *P-E* loops of **a** S1, **b** S2, **c** S3, and **d** S4 MLCCs.

Note of Fig. S10.

The polarization behavior of ferroelectric and antiferroelectric materials, such as electric polarization and hysteresis, is determined by the chemical and phase composition, lattice structure, domain morphology, internal stress, and so on.

In $(Pb_{0.9}Ba_{0.04}La_{0.04})(Zr_{0.65}Sn_{0.3}Ti_{0.05})O_3$ (S1), due to the larger ion radius of Ba^{2+} ions, the substitution of Ba^{2+} for Pb^{2+} increases the tolerance factor of the lattices, which decreases the stability of the antiferroelectric phase of S1. On the other hand, smaller La^{3+} ions replace the Pb^{2+} ions, stabilizing the

antiferroelectric phase. Meanwhile, the replacement of A-site ions in the perovskite lattices (smaller La^{3+} cations occupy A-sites of the perovskite lattices with the formation of V''_{Pb} vacancies) flattens the free-energy profile caused by the local lattice distortion and lowers the barrier of the ferroelectric-antiferroelectric phase transition, depressing the hysteresis of the material. The synergetic effects of the substitution of Ba^{3+} and La^{3+} for A-site Pb^{2+} enable S1 favorable polarization with a slim *P-E* loop (Fig. 2d).

The high polarization (~77 μC cm^{-2}) of S2 originates from its multiphase transition and large ion displacement. As analyzed by the XRD result (Fig. S6), two orthorhombic phases, e.g., the O_I phase belonging to the *Pbam* space group and the O_{II} phase of the *Bmm*2 space group coexist in S2. As revealed by the *P-E* loop (Fig. S11), the two inflection points of the charge curve of the *P-E* loop at 200 kV cm^{-1} and 270 kV cm^{-1} indicate the AFE-FE_I and FE_I-FE_{II} multiphase transitions of S2, promoting the high polarization. In addition, as revealed by the HAADF-STEM (Fig. 3), the average displacement of B-site ions of S2 is larger than that of S1 and S3, which also contributes to the high polarization. Moreover, as verified by the PFM (Fig. S13,S14), the domains with a large size of S2 can be highly aligned with electric fields, the recovery of which to the original random orientation needs to consume more energy. As a result, S2 has a relatively large hysteresis and an inferior energy efficiency.

In S3, the Ca^{2+} and Sn^{4+} ions replace the A- and B-sites Pb^{2+} and Zr^{4+} ions, respectively, and induce a highly diffused AFE-PE phase transition. As a result, S3 shows a linear-like slim *P-E* loop with a very low hysteresis (Fig. 2d). Also because of the diffused phase transition, the polarization of S3 is significantly depressed.

Interestingly, with the periodically heterogeneous lamination structure, S4 shows a high polarization and low hysteresis simultaneously. As rationalized by the phase-field simulation (Fig. 4), with the

interlaminar strain engineering, the tensile stress decreases the domain size of S2 and depresses its hysteresis, while the compressive stress increases the displacement of the B-site ions and enhances the polarization of S1 and S3. Eventually, S4 possesses both high energy storage density and efficiency.

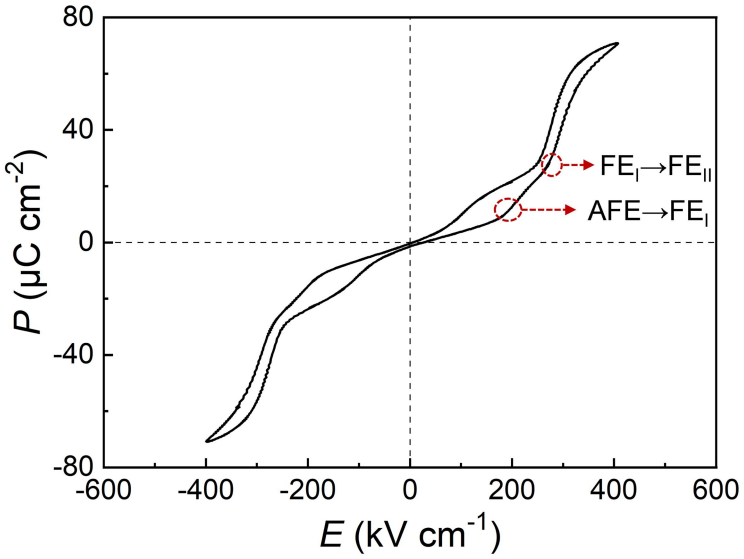

Fig. S11 | The *P-E* Loop of the antiferroelectric with multiphase transitions.

Note of Fig. S11.

It is accepted that phase transitions induced by electric fields generate large electrostrain in ferroelectric (FE) and antiferroelectric (AFE) materials[19-21]. Different from S1 and S3 has only a simple AFE-FE phase transition during the charging process, the two inflection points of the charge curve of the *P-E* loop at 200 kV cm^{-1} and 270 kV cm^{-1} indicate the AFE-FE_I and FE_I-FE_{II} multiphase transitions of S2. It is believed that the multiphase transition behavior contributes to the large strain of S2. The multiphase transition behavior is also observed in S4 (Fig. S12).

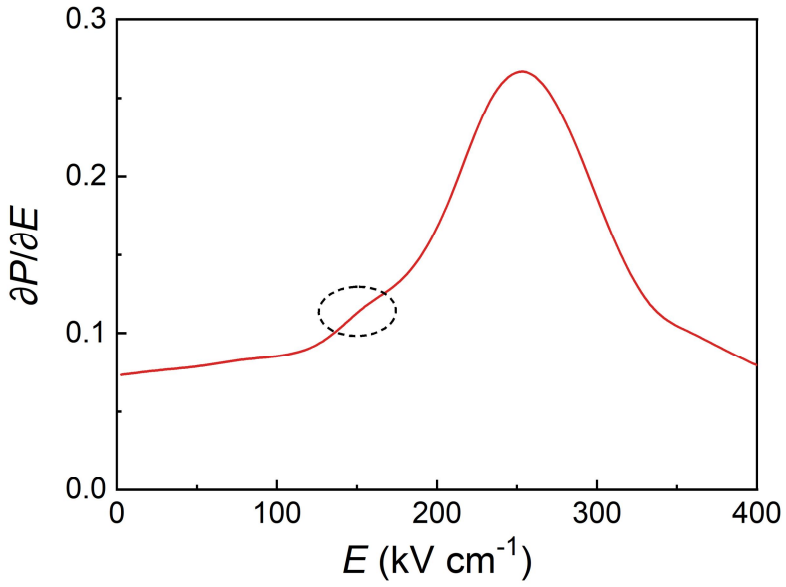

Fig. S12 | The *∂P*/*∂E* curve of S4 extracted from its corresponding *P*-*E* loop during the charging process. In S4 MLCC, S1 and S2 layers have different AFE-FE phase transition fields, and especially, the two inflection points of the charge curve of the *P*-*E* loop at 200 kV cm^{-1} and 270 kV cm^{-1} indicate the complex AFE-FE_I and FEI-FE_{II} multiphase transitions of S2. As S4 MLCC is composed of S1, S2 and S3 ceramic layers, it should exhibit multiple field-induced phase transition behavior. The hump at 150 kV cm^{-1} (cycled by the dashed line) and the peak at 253 kV cm^{-1} signify the multiple-phase transition behavior of S4.

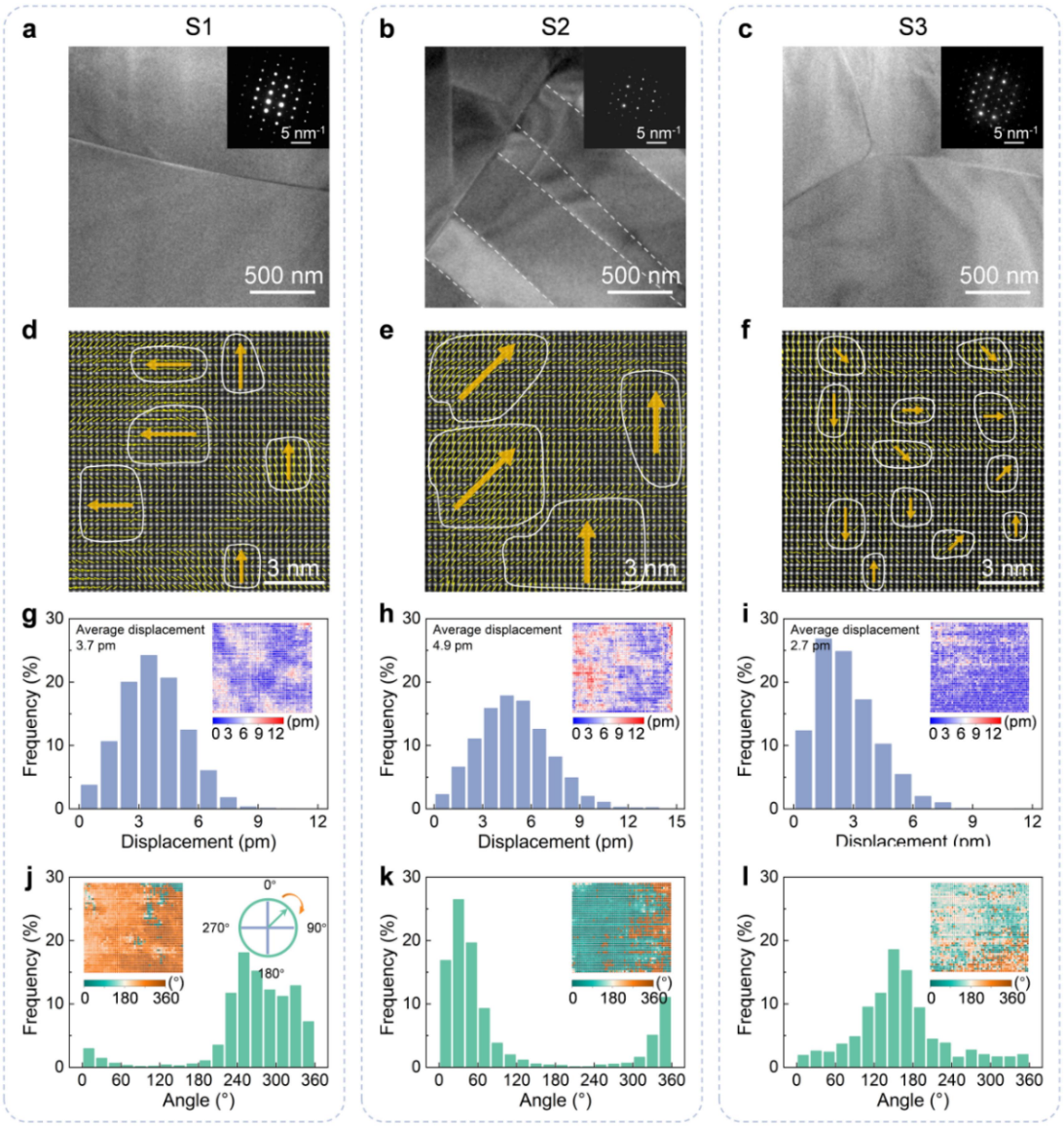

Fig. S13 | Domain structures of the materials in S4 MLCC. BF-TEM images of **a** S1, **b** S2, and **c** S3 in S4 MLCC. The insets show the corresponding SAED patterns along the [110] zone axes. Atomic-scale HAADF-STEM images of **d** S1, **e** S2, and **f** S3 in S4 MLCC along the [110] zone axes. Displacement magnitude distribution histograms of **g** S1, **h** S2, and **i** S3 in S4 MLCC. The insets show the corresponding atomic displacement magnitude mappings. Vector angle distribution histograms of **j** S1, **k** S2, and **l** S3 in S4 MLCC. The insets show the corresponding atomic displacement angle mappings.

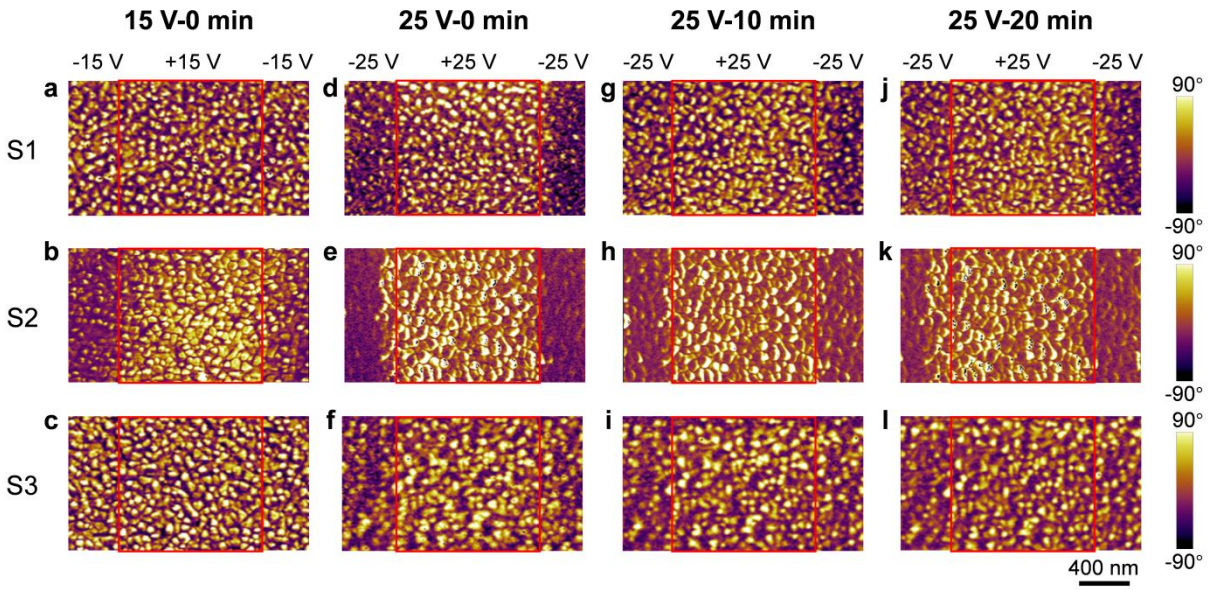

Fig. S14 | Out-of-plane PFM phase images under different voltages and relaxation times for S1-S3. **a-c** PFM phase images under ±15 V. **d-f** PFM phase images under ±25 V. **g-i** PFM phase images after a 10-minute relaxation time following the removal of the ±25 V voltage. **j-l** PFM phase images after a 20-minute relaxation time following the removal of the ±25 V voltage.

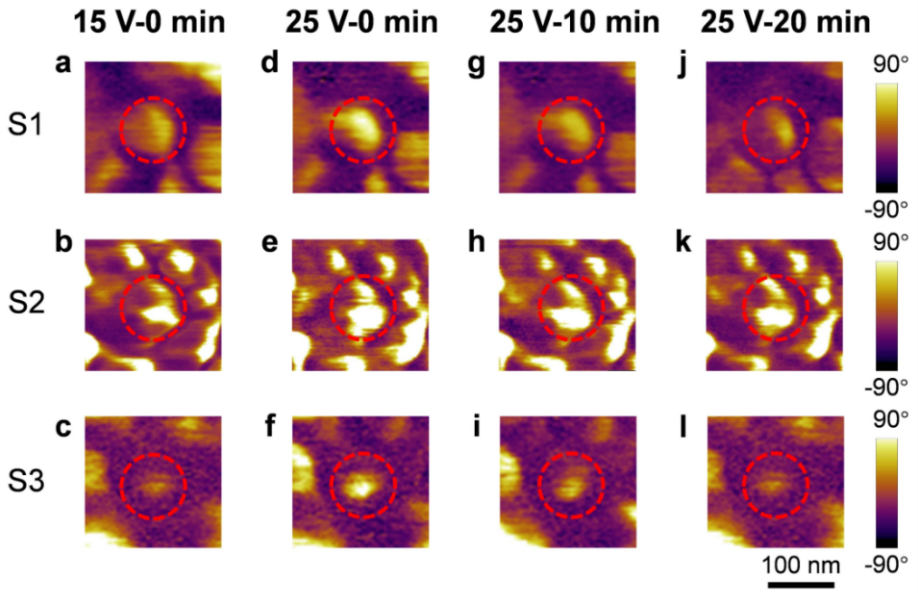

Fig. S15 | Out-of-plane PFM phase images and domain evolution under different voltages and relaxation times for S1-S3. a-c PFM phase images under 15 V. **d-f** PFM phase images under 25 V. **g-i** PFM phase images after a 10-minute relaxation time. **j-l** PFM phase images after a 20-minute relaxation time.

In the measurement, voltages of 15 V and 25 V were applied to the specimens in the red cycled region, and the out-of-plane phase images are presented in Fig. S15. With a relatively low voltage of 15 V, no obvious domain switching can be observed in S1 and S3, while the domains in S2 are aligned with the field (Fig. S15a-c). We then increased the voltage to 25 V, and it can be seen that small domains begin to align with the voltage in S1 and S3 (Fig. S15d,f), and large domains with a high degree of orientation are formed in S2 (Fig. S15e). The high compliance of the domain with applied fields enables S2 a higher polarization compared with that of S1 and S3, as evidenced by the *P-E* loops (Fig. 2d). Moreover, with a larger size, the domains in S2 have a longer relaxation period. As shown in Fig. S15d-l, the orientation of the domains in S2 can be maintained longer than 20 mins after

withdrawing the voltage (Fig. S15k), while the domains in S1 and S3 began to get back to their original orientation after 10 mins (Fig. S15g,i). The large domain size results in the high hysteresis of S2 as evidenced by its *P*-*E* loop (Fig. 2d), leading to its inferior energy storage efficiency.

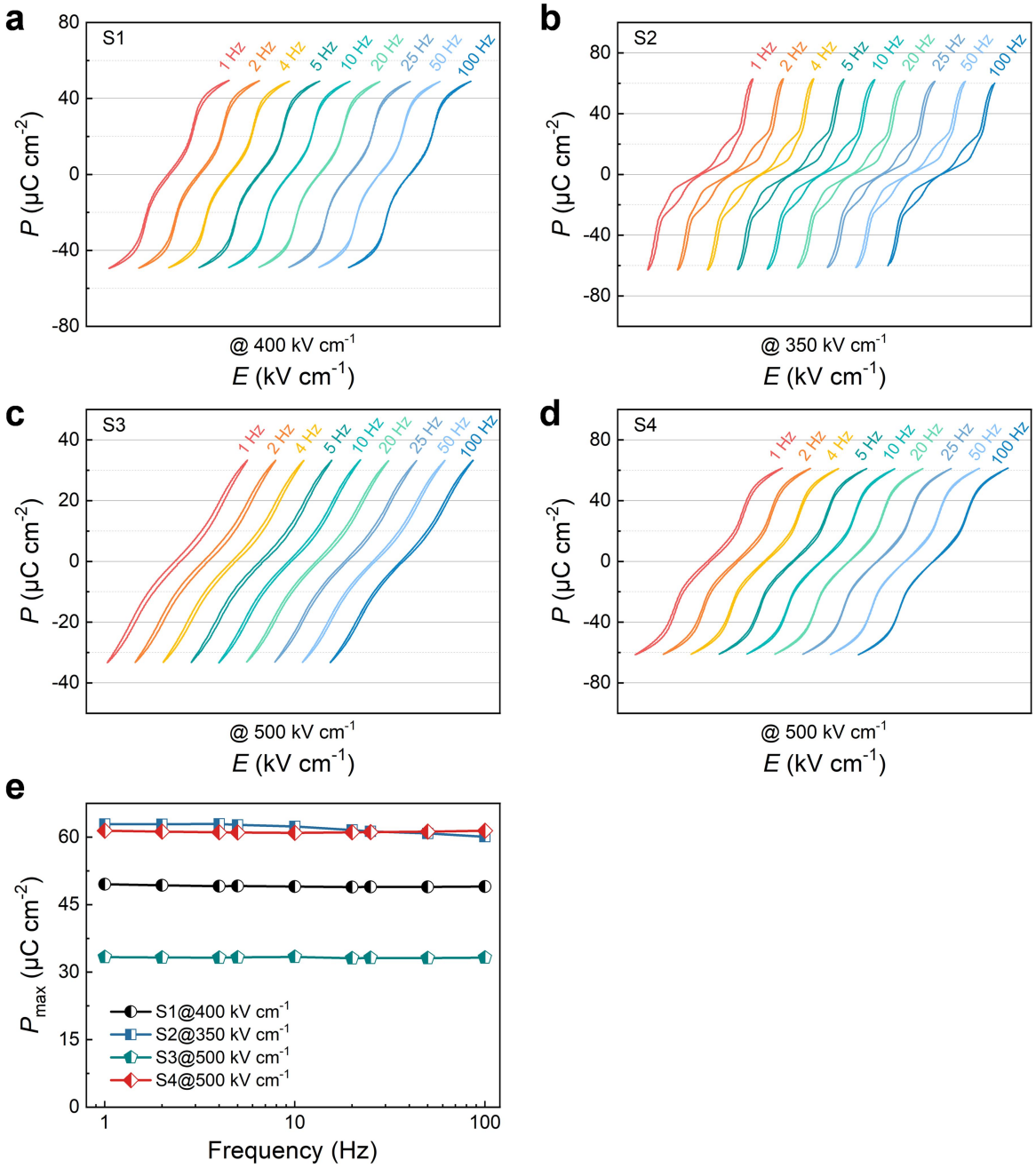

Fig. S16 | Polarization loops of S1-S4 MLCCs measured with different frequencies. a-d *P-E* loops of S1-S4 MLCCs with various testing frequencies. **e** Polarization of the samples as a function of frequency at room temperature. The polarization of the MLCCs is independent of frequency.

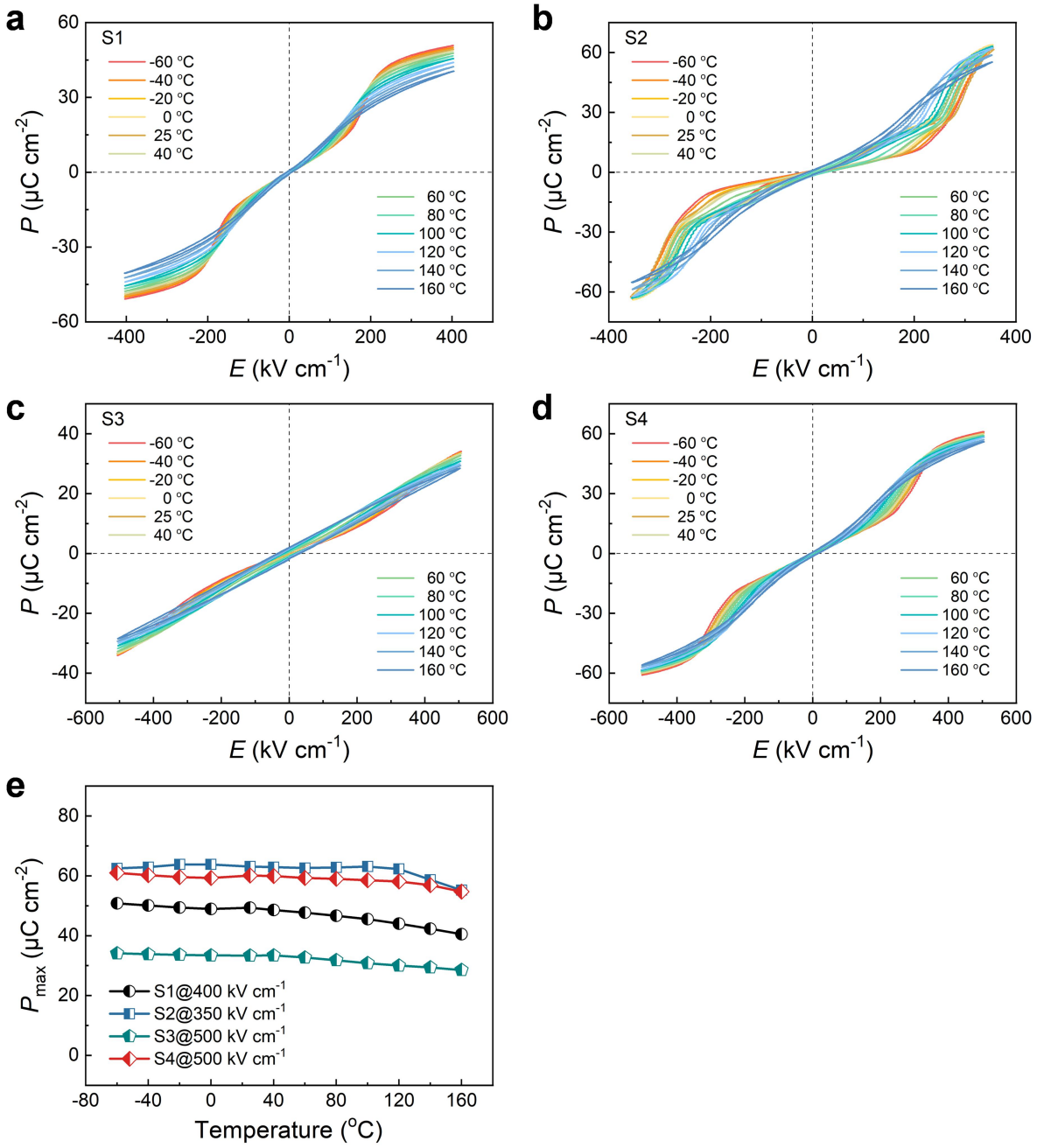

Fig. S17 | Temperature stability of S1-S4 MLCCs. a-d *P-E* loops of S1-S4 MLCCs at different temperatures. **e** Polarization of S1-S4 MLCCs as a function of temperature.

Due to the diffused partial AFE orthorhombic (AFE_O)-paraelectric cubic (PE_C) phase transition indicated by the flat dielectric constant-temperature curve (Fig. 2c), the polarization of S3 is almost

independent of temperature (Fig. S17e). With a diffusive AFE tetragonal (AFE_T)-PE_C phase transition at ~150 ℃ and the multistage phase transitions [AFE_{OI} (orthorhombic structure with space group of *Pbam*)-AFE_{OII} (orthorhombic structure with space group of *Bmm*2), AFE_{OII}-PE_{MCC} (paraelectric multicell cubic), and PE_{MCC}-PE_C phase transitions], respectively, the polarization of S1 and S2 decrease moderately with the increase of temperature. When laminated as S4 (Fig. 1a), the MLCC has a stable polarization as a function of temperature with the interlaminar strain engineering, as shown in Fig. S17d,e. Moreover, the hysteresis of S4 is low in the whole temperature range. The stable polarization with the low hysteresis allows S4 to exhibit high energy storage stability. As shown in Fig. 5e, the recoverable energy density and energy efficiency of S4 MLCC change less than ±13% in the temperature span ranging from −60 ℃ and 160 ℃, meeting the X8R industrial standard for MLCCs (the performance changing within ±15% over a temperature range of −55 ℃ to 150 ℃).

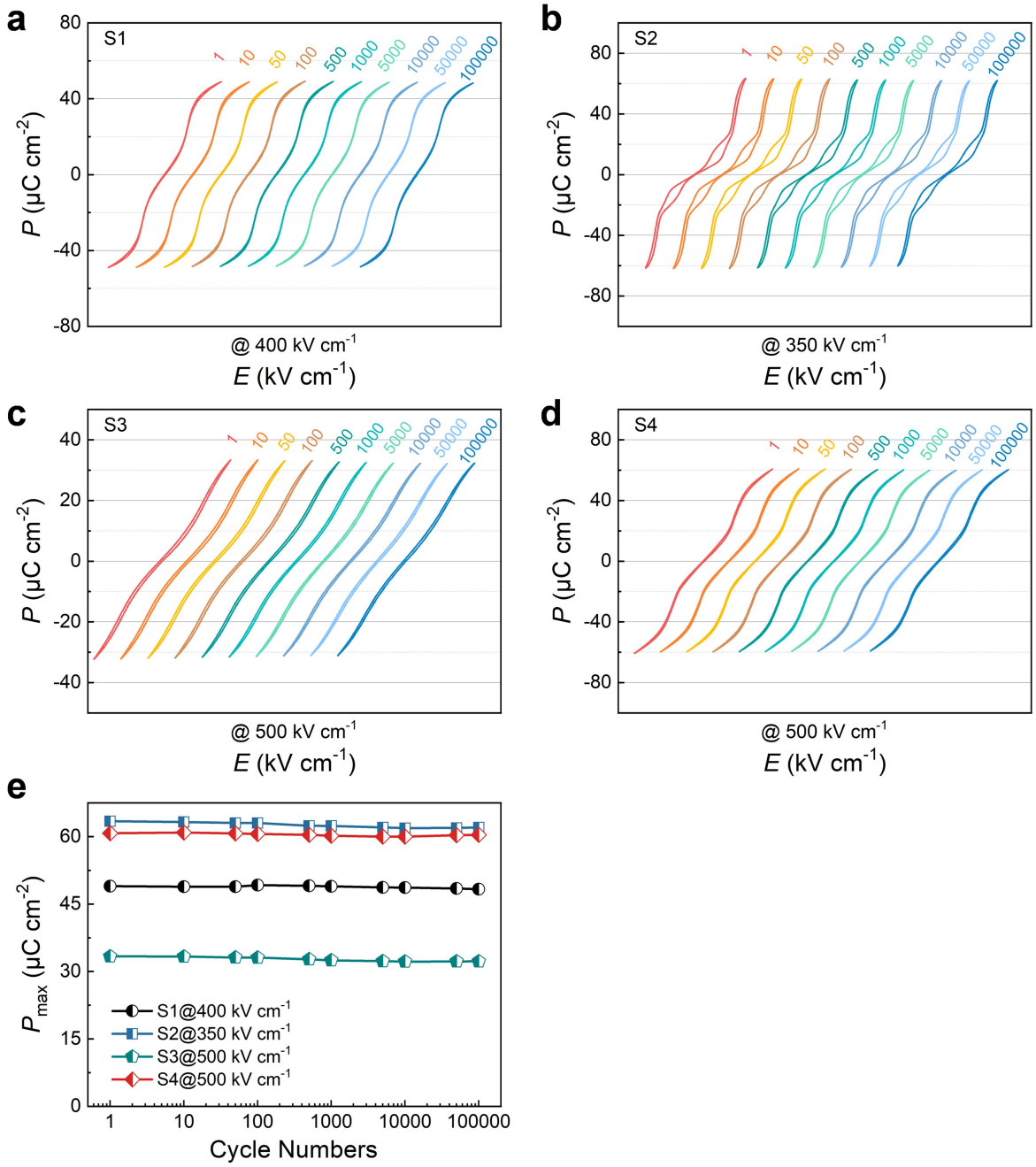

Fig. S18 | Cycling stability of S1-S4 MLCCs. a-d *P-E* loops of S1-S4 MLCCs with the cycling measurement. **e** Polarization of S1-S4 MLCCs in the cycling measurement.

It is clear that the polarization and hysteresis of all of the MLCCs change marginally over 100,000 cycles. For example, as shown in Fig. S18e, the polarization of S4 is ~60 μC cm^{-2} after being subjected

to 100,000 charge-discharge cycles, which maintains the same value as that tested at the original state. Therefore, all of the MLCCs, including S1-S4, show no obvious decay of energy storage density and efficiency calculated with the *P*-*E* loops in the cyclability measurements. For instance, as shown in Fig. 5f, S4 shows a fatigue-free energy storage density of 14.3 ± 0.3 J cm^{-3} and an efficiency of 95.4 ± 0.4% in the cycling measurement.

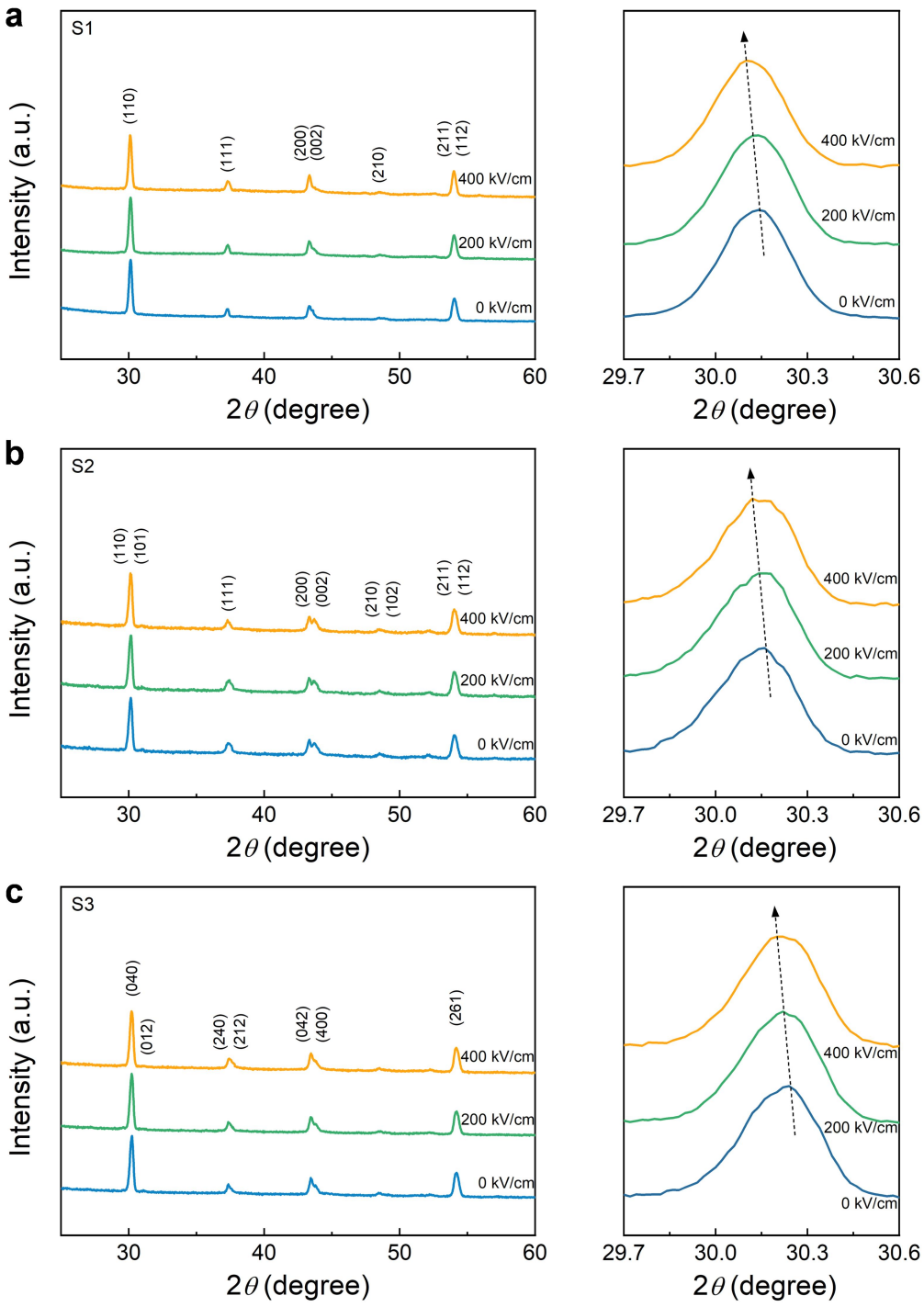

Fig. S19 | XRD patterns of S1-S3 under different electric fields. The XRD patterns and enlarged characteristic peaks at 2θ = 29.7°-30.6° of **a** S1, **b** S2, and **c** S3 under electric fields ranging from 0 kV cm^{-1} to 400 kV cm^{-1}.

Microscopically, the deformation of lattices under electric fields plays an important role in the macroscopic strain. To evaluate the lattice deformation induced by electric fields, we performed an in-situ X-ray diffraction (XRD) measurement on S1-S3 applied with various electric fields. As shown in Fig. S19, the characteristic peaks of S1-S3 located at ~30° shift toward the low degree with the increase of the electric field, indicating the lattice volume of the ceramics increases with the increased field. Calculated with the Rietveld refinement method and the Generalized Structure and Analysis Software (GSAS) based on XRD data[15], the lattice parameters of S1-S3 under 0 kV cm^{-1} and 400 kV cm^{-1} are listed in Table S3. It can be seen that with an electric field of 400 kV cm^{-1}, the lattice volume of S2 increases by 0.53% in comparison with that without an electric field, the deformation is significantly larger than that of S1 and S3. Thus, S2 possesses a significantly larger strain than that of S1 and S3. Moreover, as verified by the PFM (Figs. S14 and S15), the domains of S2 are highly aligned with electric fields, the switching of which also contributes to the large strain.

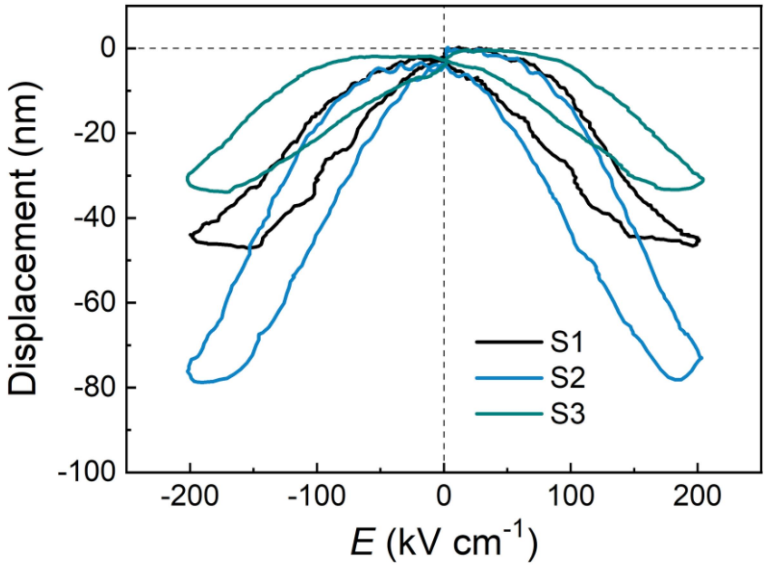

Fig. S20 | Transverse displacement of S1, S2, and S3.

To investigate the stress direction of the dielectric layers in the S4 MLCC, besides evaluating the strain along the longitudinal direction (*z*-axis direction, paralleled to the applied electric field, Fig. 4a of the main text), we measured the displacement of S1, S2 and S3 bulks along the transverse direction perpendicular to the applied field (Fig. S21). As shown in Fig. S20, the negative displacements signify that all of S1, S2, and S3 constrict along the transverse direction (perpendicular to the applied field) with the applied field. Moreover, the absolute value of displacement of S2 is larger than that of S1 and S3, indicating that S2 is subjected to a tensile stress while S1 and S3 are subjected to compressive stresses in S4 under electric fields with the electrostrictive effect.

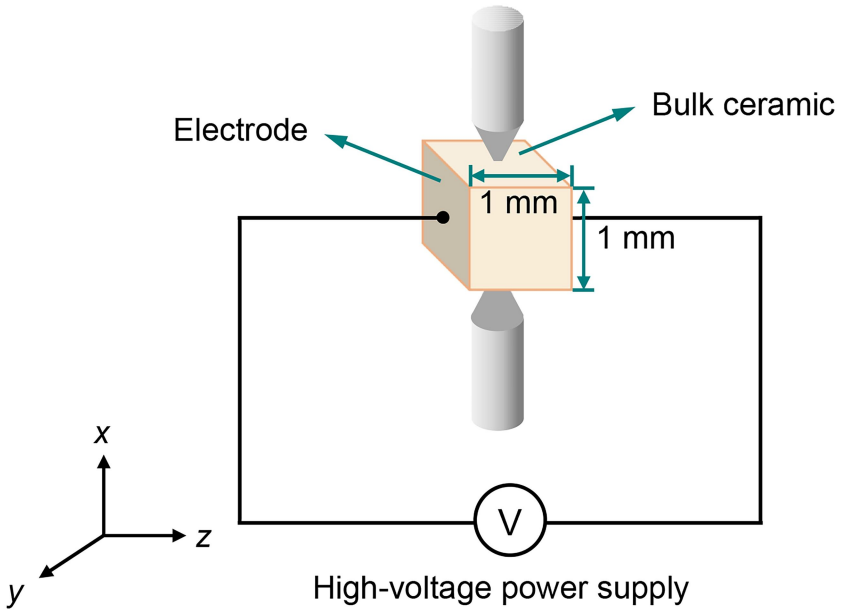

Fig. S21 | Schematic diagram of transverse displacement measurement. The applied electric field is along the *z*-axis direction, while the displacement is measured along the *x*-axis direction. The displacement change of the sample is measured by an external laser interferometer.

Note S3. Comparison of interlaminar stress of the heterogeneous layered structures without and with internal electrodes.

Fig. 2a exhibits the cross-section SEM images of the MLCCs, and it can be seen that the ceramic layers with a thickness of 8 μm were well connected with the internal 70Ag-30Pd electrodes (700 nm). To enhance the binding force between the electrodes and the ceramic layers, and bridge the gap of the coefficients of thermal expansion between the electrodes and the ceramics, 10 wt.% of ceramic powders were added to the electrode slurry in our experiment. We then performed a pull-off measurement to test the binding force between the electrodes and the ceramic layers. In the measurement, metal pins were welded with the Ag/Pd electrodes on the surface of S1, S2 and S3 ceramics, and a tension force along the normal direction was applied. Table S5 lists the adhesion strength (the minimum force for pulling the electrodes off from the ceramic thick films) between the electrodes and ceramic layers. S1, S2 and S3 have relatively high adhesion strengths of 12.2 MPa, 10.9 MPa and 10.7 MPa with the metal electrodes, as compared with those of ceramics reported in the literature[22]. The high adhesion strength indicates that the influence of the metallic electrodes on the in-plane strain between the ceramic layers of the MLCCs would be limited.

To evaluate the effect of the electrodes on the interlaminar strain more intuitively, we calculated and compared the interlaminar stresses between the ceramic layers of S4 MLCC with and without metal electrodes via finite element analysis (FEA). In the model (Fig. S22), C3D8R mesh was used to ensure that each layer of the ceramic has at least 3 grids along the thickness direction (Fig. S22b,c). With a rigid contact between the layers, the model defines the interaction relationship between each layer through a tie constraint. According to the results of quasi-static compression experiments, the model sets the properties of each layer of material by the linear elastic model. For the simulation, Young's

moduli of S1, S2, and S3 ceramics are measured (16.35 GPa, 22.86 GPa and 19.65 GPa, respectively). The Young's modulus of the metal electrodes is 86.8 GPa [Ref. 23]. The Poisson ratios of S1, S2, S3 and the metal electrode are 0.27, 0.33, 0.27, and 0.48, respectively[24,25]. With a total strain of 0.16% along the *z* direction (the thickness direction) with an electric field of 400 kV cm^{-1} as we tested in S4 MLCC (Fig. 4a), we applied strains of 0.19%, 0.31% and 0.11% (equally scaled with the strain values we tested in S1, S2 and S3 MLCCs) on S1, S2 and S3 of S4 for the simulation (the equivalent displacements of S1, S2 and S3 are 0.061 μm, 0.042 μm, and 0.011 μm, as shown in Fig. S23a,b). As shown in Fig. S23c,d, the simulation result indicates that the stresses on the ceramic layers with and without electrodes have little difference. For example, the maximum stress between the ceramic layers in S4 with and without electrodes are 44.5 MPa and 46.2 MPa, respectively. Therefore, it is believed that the favorable performance of S4 including the high energy storage density and the efficiency could be attributed to the interlaminar strain engineering as rationalized by the phase-field simulation.

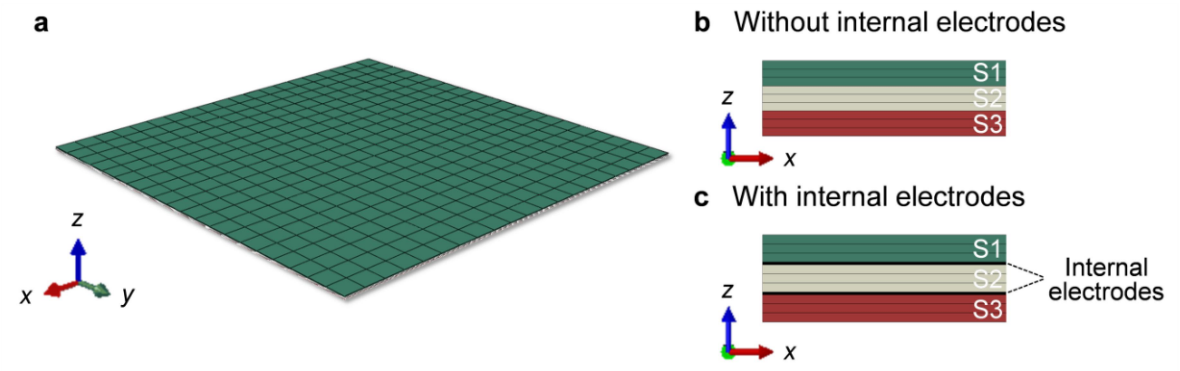

Fig. S22 | Finite element model and schematic diagrams of heterogeneous layered structures. a Finite element model of the heterogeneous layered structure. **b,c** Schematic diagrams of heterogeneous layered structures without and with internal electrodes.

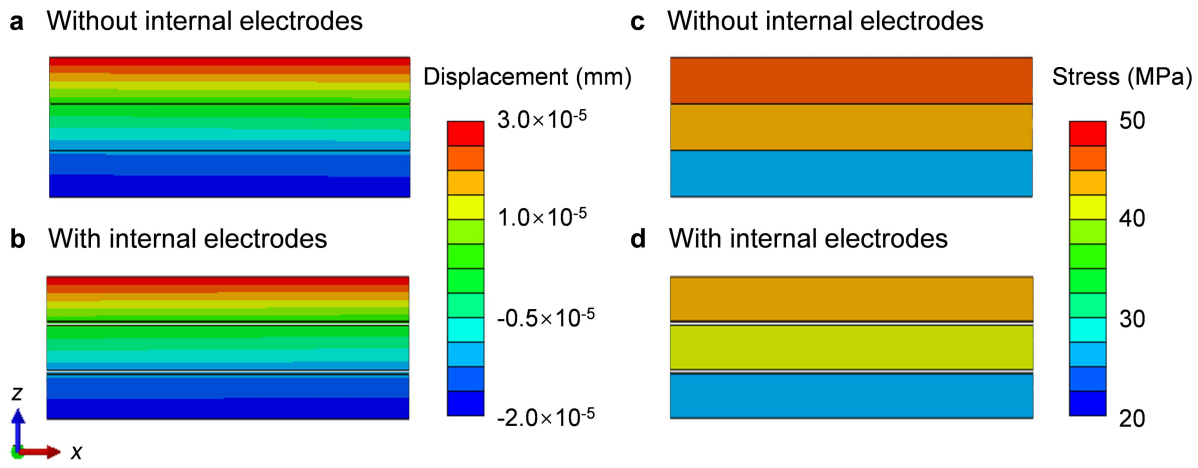

Fig. S23 | Mechanical response of the heterogeneous layered structures without and with internal electrodes. **a,b** *z*-direction displacement distribution and **c,d** stress distribution across local cross-sections.

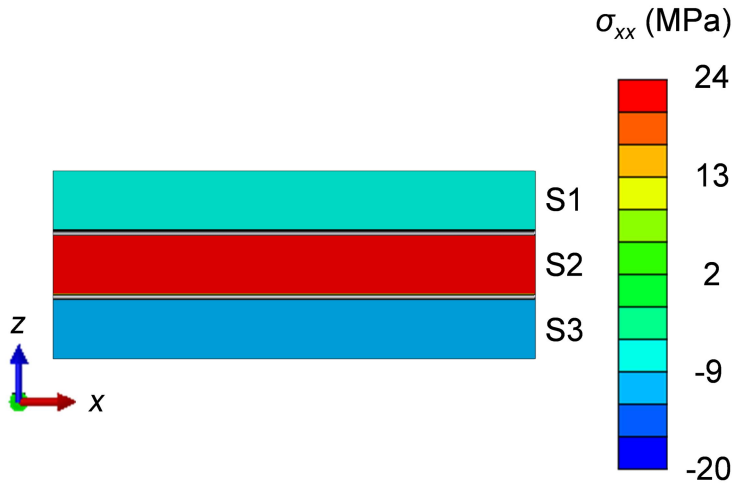

Fig. S24 | Stress on the ceramic layers of S4 MLCC along the *x*-axis direction induced by the electrostrictive effect.

Note of Fig. S24.

The FEA simulation results shown in Fig. S23 represent the equivalent stress calculated with the formula[26]:

$$\sigma_e = \frac{1}{\sqrt{2}}\sqrt{(\sigma_{xx}-\sigma_{yy})^2+(\sigma_{yy}-\sigma_{zz})^2+(\sigma_{zz}-\sigma_{xx})^2+6(\tau_{xy}^2+\tau_{yz}^2+\tau_{xz}^2)} \quad (12)$$

where σ_{xx}, σ_{yy}, and σ_{zz} are the normal stresses along the *x*, *y*, and *z* directions, respectively, and τ_{xy}, τ_{xz}, and τ_{yz} are the shear stresses.

To examine the in-plane stress of the ceramic layers induced by the electrostrictive effect in MLCCs, the stress along the *x* direction of S4 MLCC simulated using FEA is presented in Fig. S24. The results indicate that S1 and S3 layers are subjected to compressive stress (denoted by the negative value of σ_{xx}) while S2 layer is subjected to tensile stress (signified by the positive value of σ_{xx}). The ceramic layers of the MLCC are subjected to a similar *y*-direction stress as that along the *x* direction due to the symmetry of the model.

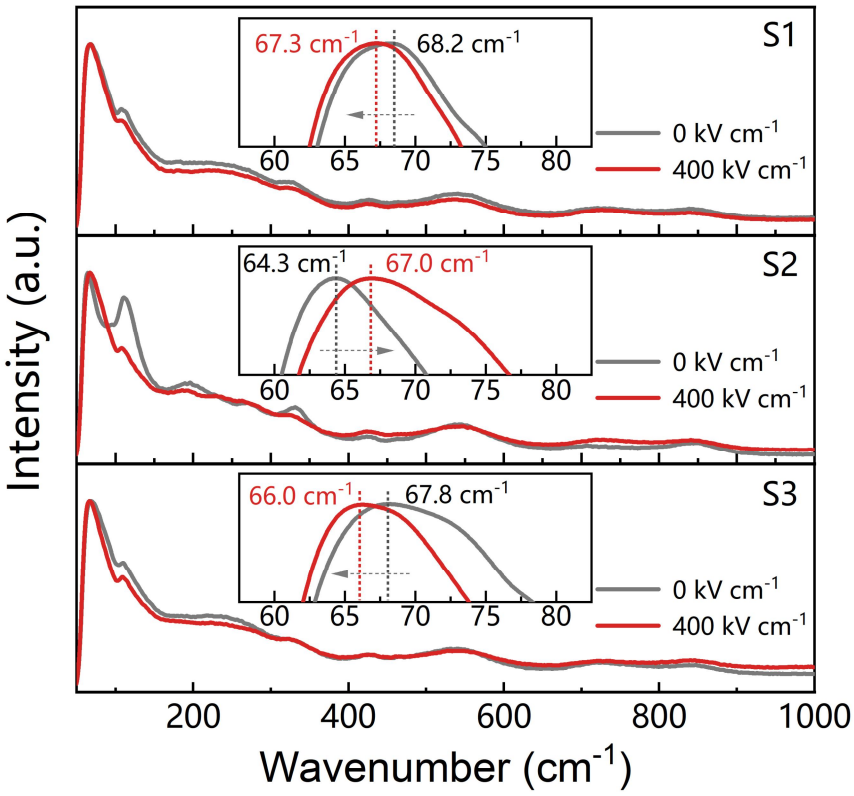

Fig. S25 | In-situ Raman spectra of the S1-S3 layers in S4 MLCC. Raman measurements were performed on the S1, S2, and S3 layers in S4 MLCC to determine the shift of the Raman peak positions. The Raman spectra were collected at the dielectric layer under electric fields of 0 kV cm^{-1} and 400 kV cm^{-1}.

Note of Fig. S25.

Raman spectroscopy is an effective technique to analyze the microstructure of a material by measuring the inelastic scattering (Raman scattering) of incident photons interacting with the molecules in materials[27]. Raman scattering is caused by the inelastic collision of photons with molecules, leading to a frequency shift of the scattered light. The frequency (wavenumber) shifts reflect the change of lattice vibrational modes in the material. For ferroelectric/antiferroelectric ceramics, Raman

spectroscopy is utilized to evaluate the interatomic spacing and lattice distortion originating from doping or internal stress, as the vibration frequencies of the Raman spectroscopy shift with the change of lattice parameters. For example, the scattering peak shifts toward low frequency (low wavenumber) as the interatomic spacing increases[27]. Therefore, we performed the in-situ Raman measurement on S4 applied with an electric field of 400 kV cm^{-1}, and compared the Raman spectroscopies of S1, S2 and S3 layers that make up the S4 MLCC without and with electric fields. The schematic diagram of in-situ Raman measurement is shown in Fig. S26.

The stress (σ_{ij}) induced by the electric field in MLCCs can be evaluated using $\Delta\omega = \Pi_{ij}\sigma_{ij}$, where $\Delta\omega$ is the Raman frequency shift, and Π_{ij} is a second-rank tensor defined as the piezospectroscopic (PS) coefficient, representing the shift in the Raman peak wavenumber per unit stress[28,29]. The PS coefficient for lead zirconate titanate (PZT)-based ceramics is ~0.028 cm^{-1} GPa^{-1} [Ref. 30,31]. As $\Delta\omega$ of S1, S2, and S3 in S4 are 0.9 cm^{-1}, 2.7 cm^{-1}, and 1.8 cm^{-1} under an electric field of 400 kV cm^{-1}, respectively (Fig. S25), the calculated stresses of S1, S2, and S3 are 32.1 MPa, 96.4 MPa, and 64.3 MPa, respectively. The stresses calculated by the in-situ Raman agree with the stresses calculated with the FEA (~45 MPa, Fig. S23d) in the same order of magnitude.

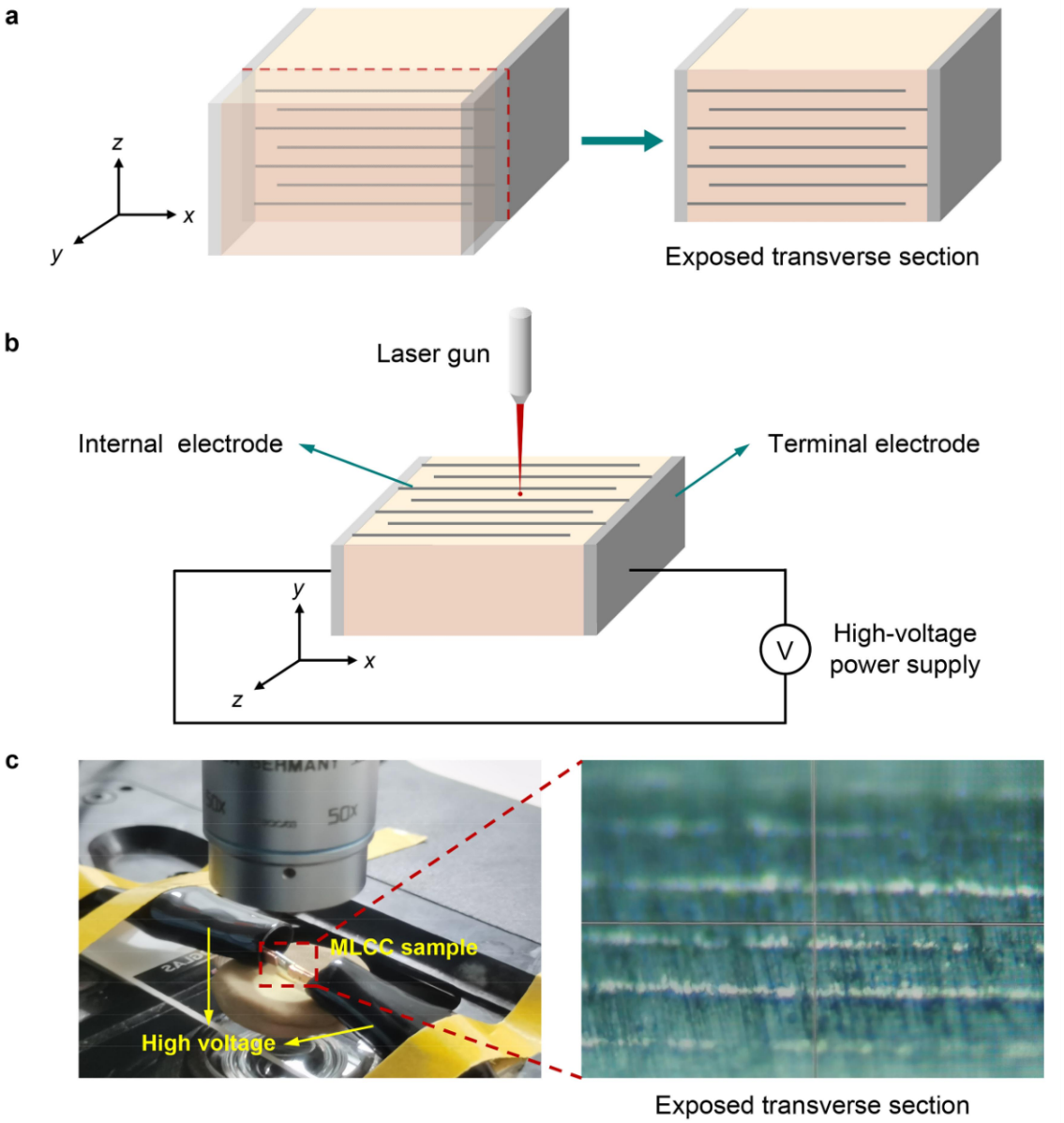

Fig. S26 | Schematic diagram of in-situ Raman measurement. a A MLCC sample cut along the red dash line for the in-situ Raman measurement. **b** Schematic diagram of the in-situ Raman measurement. **c** Photos of the instrument for the in-situ Raman measurement.

Note S4. The impact of thermal expansion on the interlaminar strain engineering.

The stress/strain plays an important role in tuning the ferroelectric/antiferroelectric properties and energy storage performance of the materials. For example, the compressive stresses with different directions, e.g., in-plane and out-of-plane, shift the field for the antiferroelectric-ferroelectric phase transition and change the polarization of the ceramics[32]. Hydrostatic pressure could transit the ferroelectric (Pb,La)(Zr,Ti)O_3 to the antiferroelectric phase, and meanwhile, decrease the maximum and remnant polarizations[33]. Moreover, the compressive stress depresses the hysteresis of ferroelectric and antiferroelectric ceramics. Different from compressive stress, the out-of-plane tensile stress increases the dielectric constant and polarization of ferroelectric and antiferroelectric ceramics[34-38].

In MLCCs, the internal stress between the metal electrodes and the ceramic layers is generated during the high-temperature cofiring process due to their different coefficients of thermal expansion (CTE). To evaluate the influence of the stress produced by the mismatch of CTE in S4 MLCC on the interlaminar strain engineering, the FEA simulation was carried out. In our experiment, 10 wt.% of ceramic powders were added in the 70Ag-30Pd electrode slurry to enhance the binding force between the electrodes and the ceramic layers and reduce the difference of CTE between the electrodes and the ceramics. The method of introducing ceramic powders into the electrode slurries has been widely used in the MLCC fabrication process to enhance the thermal expansion matching rate of internal electrodes and dielectric layers[39,40]. In the FEA model (Fig. S22), C3D8R mesh was used to ensure that each ceramic layer has at least 3 grids along the thickness direction (Fig. S22b,c). With a rigid contact between the layers, the model defines the interaction relationship between each layer through a tie constraint, while the face center of the heterogeneous layered structure is fixed. For the simulation, Young's moduli of S1, S2, and S3 ceramics were measured (16.35 GPa, 22.86 GPa and 19.65 GPa,

respectively). The Young's modulus of the metal electrodes is 86.8 GPa [Ref. 23]. The Poisson ratios of S1, S2, S3 and the metal electrode are 0.27, 0.33, 0.27, and 0.48, respectively[24,25]. The thermal conductivity of S1, S2, and S3 and the metal electrodes are set as 2.1 W m^{-1} K^{-1} and 50 W m^{-1} K^{-1}, respectively[41,42]. The specific heat capacities of S1, S2, S3 and the metal electrode (500 J kg^{-1} K^{-1}, 500 J kg^{-1} K^{-1}, 200 J kg^{-1} K^{-1} and 250 J kg^{-1} K^{-1}) were measured with a differential scanning calorimeter (DSC). The CTEs of the ceramics were measured with a thermal dilatometer, and the results are shown in Fig. S27. Since the plasticity of the inner electrode increases and the rigidity of the ceramic material decreases during the high-temperature sintering process, it is accepted that thermal stress at the high sintering temperatures is low. The simulation result (Fig. S28) demonstrates that the maximum stress caused by the thermal strain mismatch is 2.3 MPa, which is ~5% that of the interlaminar stress generated by the electrostriction effect (~45 MPa, Fig. S23d). Therefore, the thermal stress caused by the mismatch of CTE could affect the interlaminar strain engineering, the polarization behavior and the energy storage performance of the S4 MLCC, nevertheless, the influence would be limited.

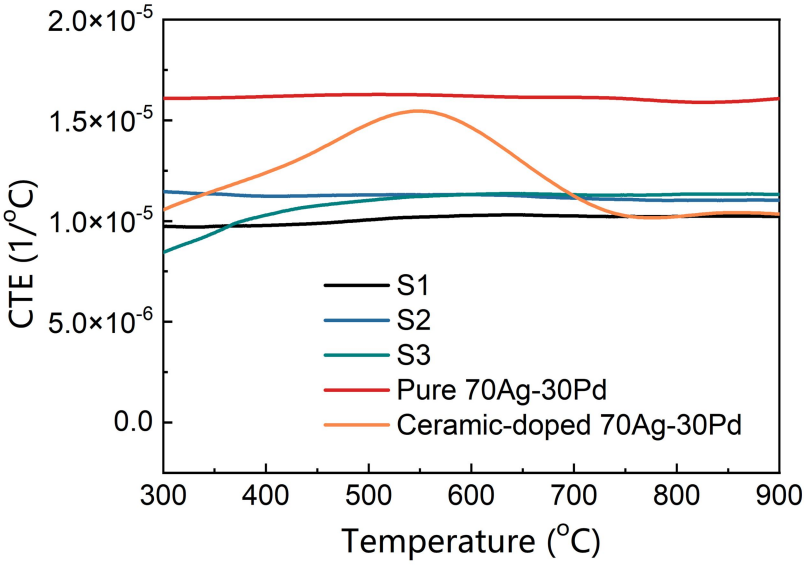

Fig. S27 | Temperature-dependent coefficient of thermal expansion (CTE) of S1-S3 dielectric layers, pure 70Ag-30Pd alloy[43], and ceramic-doped 70Ag-30Pd alloy[43].

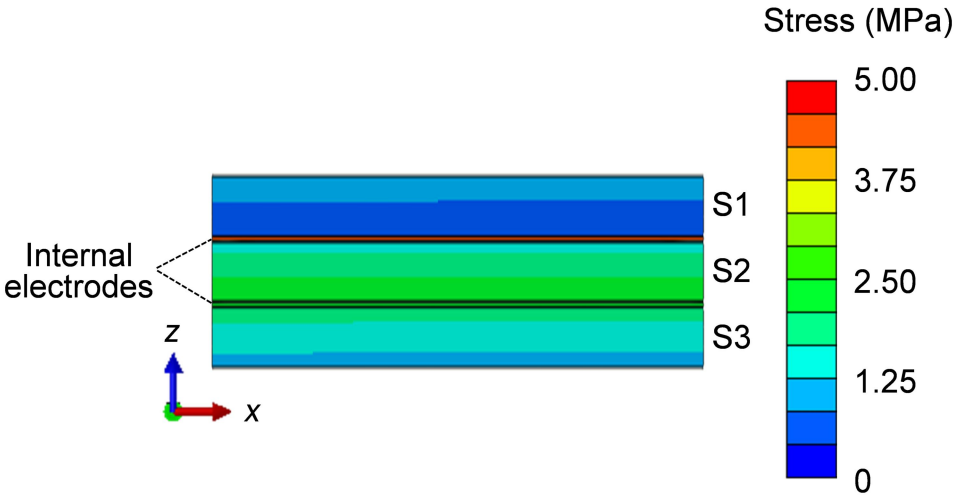

Fig. S28 | Stress distribution across local cross-sections in the heterogeneous layered structure with internal electrodes.

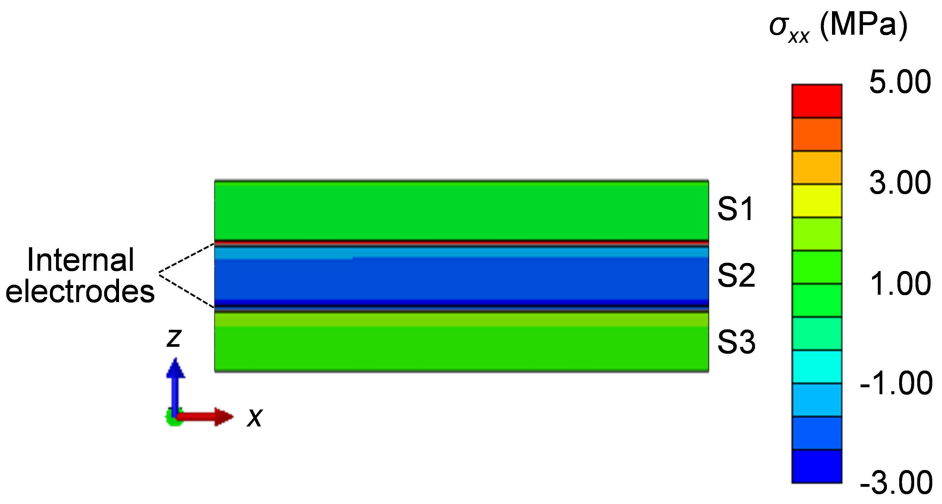

Fig. S29 | Stress on the ceramic layers of S4 MLCC along the *x*-axis direction caused by the different thermal expansions of ceramics and electrodes.

Note of Fig. S29.

The FEA simulation results shown in Fig. S28 represent the equivalent stress calculated with the formula[26]:

$$\sigma_e = \frac{1}{\sqrt{2}}\sqrt{(\sigma_{xx}-\sigma_{yy})^2+(\sigma_{yy}-\sigma_{zz})^2+(\sigma_{zz}-\sigma_{xx})^2+6(\tau_{xy}^2+\tau_{yz}^2+\tau_{xz}^2)} \quad (12)$$

where σ_{xx}, σ_{yy}, and σ_{zz} are the normal stresses along the *x*, *y*, and *z* directions, respectively, and τ_{xy}, τ_{xz}, and τ_{yz} are the shear stresses.

The stress along the *x* direction simulated by the FEA is shown in Fig. S29, where positive stress and negative stress indicate tensile and compressive stresses, respectively. The results reveal that S1 and S3 layers of S4 MLCC are subjected to tensile stresses, while S2 layers are subjected to compressive stress. Due to the symmetry of the model, the stress along the *y* direction is identical to that along the *x* direction. In addition, as no external clamping restriction is applied, it is believed that the MLCCs are in a free state along the *z* direction.

Note S5. The influence of stresses with different magnitudes on the domain structure and electric properties of ferroelectric and antiferroelectric materials.

It is well-established that stress and strain significantly influence the microstructure, such as lattice distortion and domain orientation, as well as the macroscopic properties, including phase transition behavior, polarization, electric hysteresis, dielectric constant, piezoelectric coefficient, and electrostrictive effect of ferroelectric and antiferroelectric materials. Table S6 lists the influence of stresses with different magnitudes on the domain structure and electric properties of ferroelectric and antiferroelectric materials.

For example, the longitudinal electrostrain of PZT-8 (hard PZT) and PZT-5H (soft PZT) ceramics decreases from 0.011% to 0.009% and 0.05% to 0.048%, respectively when a compressive stress of 0.5 MPa is applied on the specimens[44]. Besides, the piezoelectric coefficient of PZT ceramics increases from ~160 pC N^{-1} to ~200 pC N^{-1} as an alternating pressure increases from 0.5 MPa to 7 MPa [Ref. 45]. When the compressive stress increases to 10 MPa, the crystal lattices of (Y, Nb)-doped $BaTiO_3$ MLCCs are distorted and the domains are enlarged along the perpendicular direction to the compressive stress, leading to the increase of dielectric constant[46]. As the stress could promote the domain switching, the polarization of $Ba_{0.85}Ca_{0.15}Zr_{0.1}Ti_{0.9}O_3$ (BCZT) ceramic increases from 8.5 μC cm^{-2} at 5 MPa to 15.2 μC cm^{-2} at 40 MPa. However, as the stress increases further to a high level of 260 MPa, the polarization decreases to 11.4 μC cm^{-2}, because the domains are clamped by the large stress[47]. In antiferroelectric ceramics, for instance, compressive stress (100 MPa) could regulate the non-180° domain switching behavior of $(Pb_{0.90}Ba_{0.4}La_{0.04})[(Zr_{0.68}Sn_{0.32})_{0.86}Ti_{0.14}]O_3$ (PBLZST), moving the antiferroelectric-ferroelectric phase transition field from 14.92 kV cm^{-1} to 19.32 kV cm^{-1} and simultaneously, decreasing the polarization of the ceramic from 25.54 μC cm^{-2} to 18.02 μC cm^{-2} [Ref.

48]. In ferroelectric thin films, the compressive stress of ~3 GPa (1.7% strain) originated from the clamping of the substrate could move the Curie phase transition temperature of $BaTiO_3$ to 500 ℃, which is significantly higher than that of its ceramic bulk counterpart (~120 ℃)[49,50]. In this work, as rationalized by the FEA and the phase-filed method, moderate stresses of ~45 MPa generate in the ceramic layers of MLCCs with the electrostrictive effect, which is utilized to manipulate the domain switching behavior and optimize the energy storage performance.

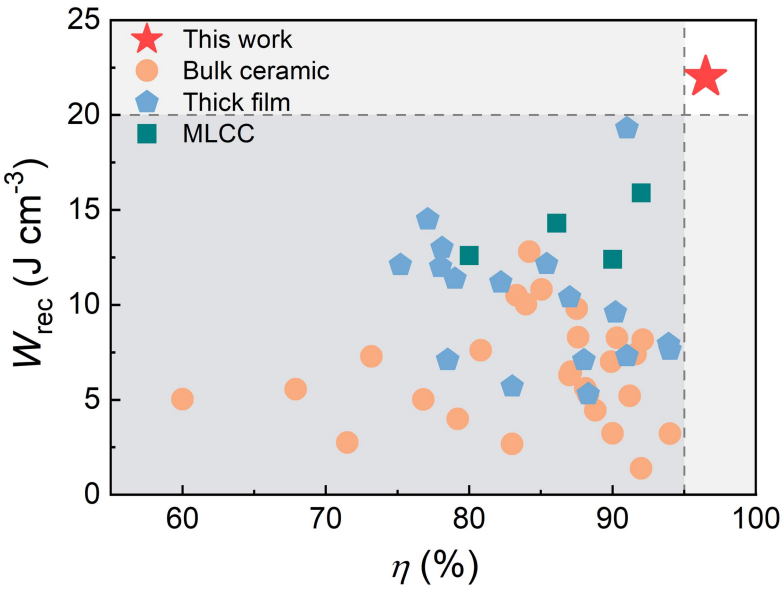

Fig. S30 | Comparison of the energy storage performance of the lead-based MLCCs. Detailed information for the lead-based materials is listed in Table S7.

Note of Fig. S30.

Fig. S30 compares the energy storage density and efficiency of typical lead-based materials, including bulks, thick films and MLCCs, and the corresponding detailed information of the materials plotted in Fig. S30 is listed in Table S7. Due to the limit of the breakdown strength, the energy storage density of most of the bulks is lower than 10 J cm^{-3}. As listed in Table S7, much higher electric fields can be applied on the materials in the forms of thick films and MLCCs. For example, with a large electric field of 760 kV cm^{-1}, a high energy storage density of 15.9 J cm^{-3} is obtained in PLCZS MLCC[51]. Simultaneously, owing to the low remanent polarization, PLCZS has a high energy efficiency of 90%. The energy storage performance of the PLCZS MLCC is similar to our S3 MLCC (Fig. 5a). Interestingly, optimized with the interlaminar strain engineering strategy, our S4 MLCC exhibits an energy storage density of 22.0 J cm^{-3} and an efficiency of 96.1%, both of which exceed the reported lead-based materials.

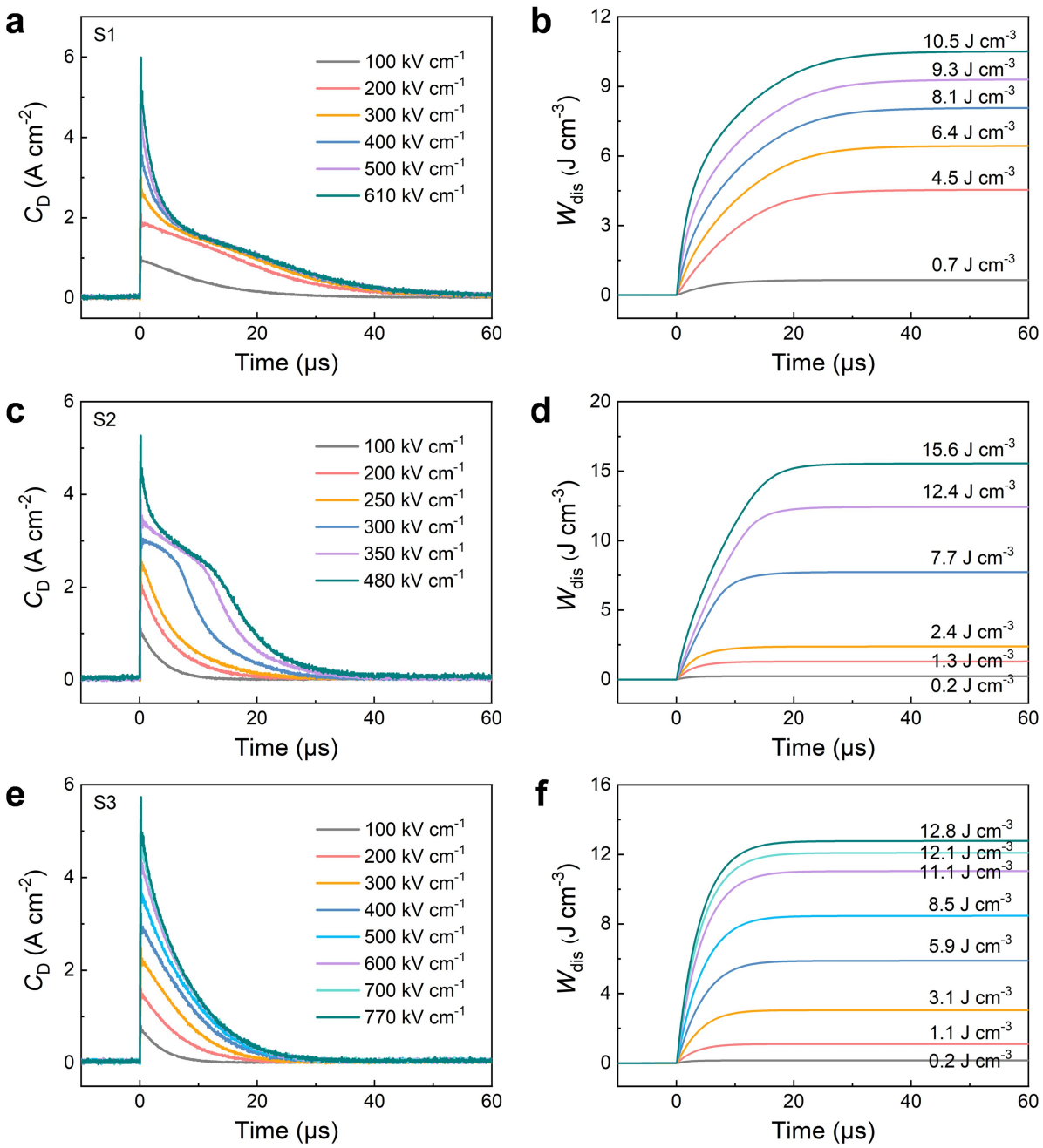

Fig. S31 | Charge-discharge performance of S1-S3 MLCCs as a function of electric field. a,**c**,**e** Current density-time curves of S1, S2 and S3 MLCCs, respectively. **b**,**d**,**f** The energy discharge behaviors of S1, S2 and S3 MLCCs, respectively.

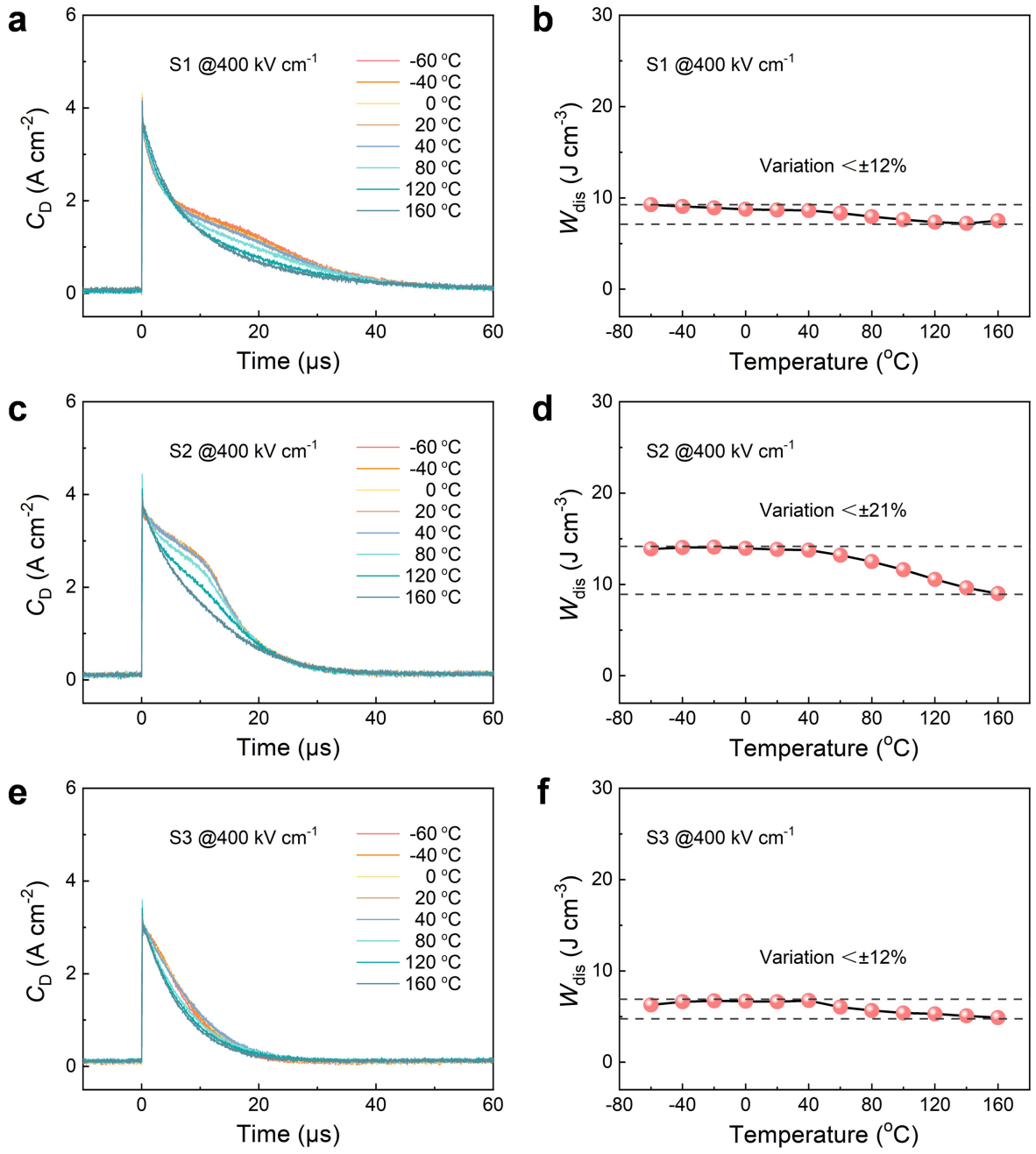

Fig. S32 | Charge-discharge performance of S1-S3 MLCCs as a function of temperature. a,**c**,**e**, Current density-time curves of S1-S3 MLCCs. **b**,**d**,**f**, The discharge energy density of S1-S3 MLCCs as a function of temperature.

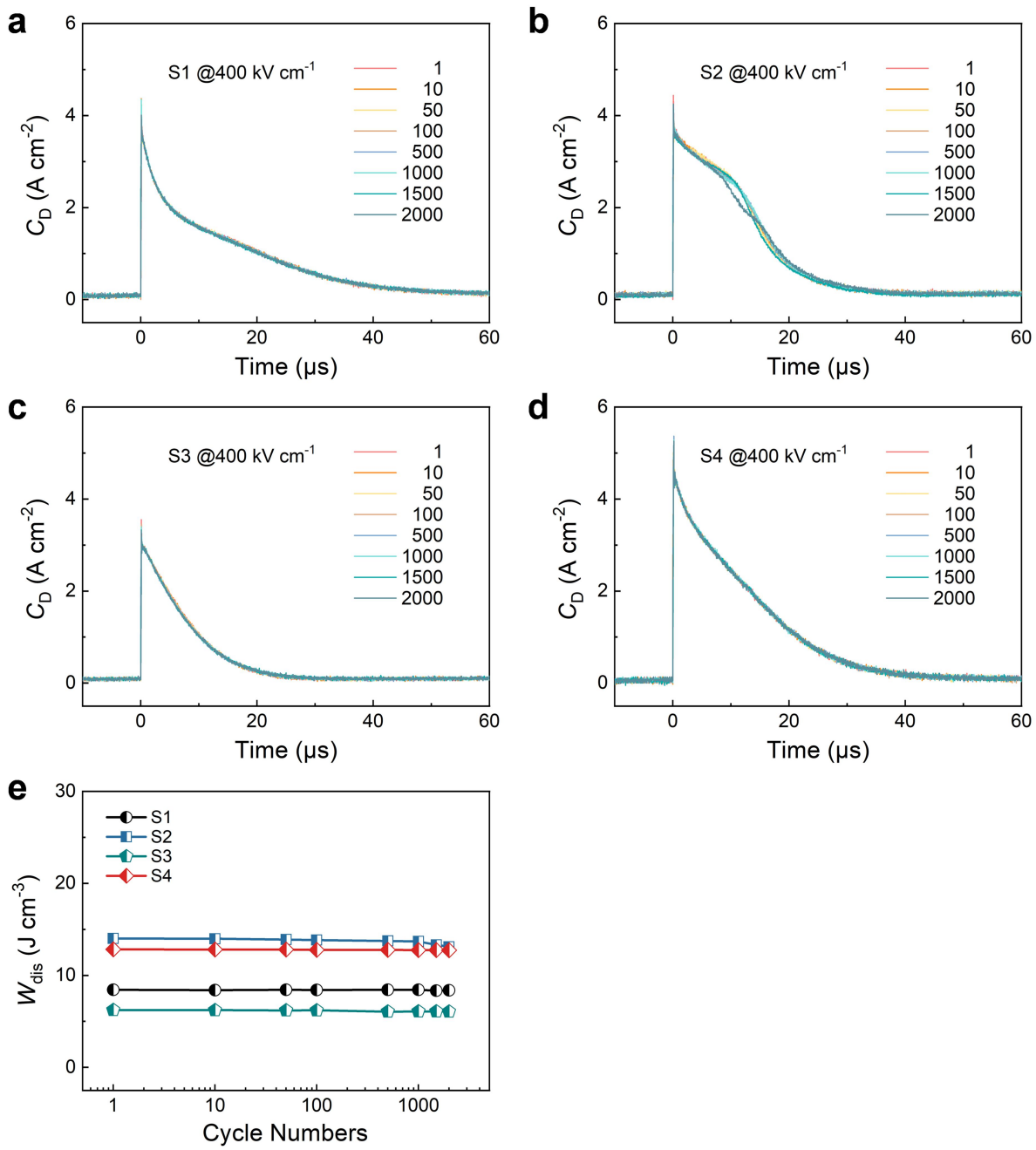

Fig. S33 | Charge-discharge performance of S1-S4 MLCCs as a function of cycle numbers. a-d Current density-time curves of S1-S4 MLCCs. **e** The discharge energy density of S1-S4 MLCCs as a function of cycle numbers.

Table S1. The complementary features of S1, S2, and S3 MLCCs. S1 and S3 MLCCs have near-zero hysteresis and remanent polarization, but their polarization is also low. In contrast, S2 MLCC possesses high polarization but relatively large remanent polarization.

Samples	P_{max} (μC cm^{-2})	P_r (μC cm^{-2})	E_b (kV cm^{-1})
S1	55.5	0.4	610
S2	77.6	0.7	480
S3	46.0	0.1	810

Table S2. Refined structural parameters by using the Rietveld method.

Samples	Space group (wt.%)	Lattice parameters (Å)	R_p (%)	χ^2
S1	*P*4*mm*	*a* = 4.1181 *b* = 4.1181 *c* = 4.0973	6.02	1.455
S2	*Pbam* (80.8%)	*a* = 5.8087 *b* = 11.6350 *c* = 8.1728	5.56	1.249
	*Bmm*2 (19.2%)	*a* = 5.8212 *b* = 4.0852 *c* = 5.8144		
S3	*Pbam*	*a* = 5.8220 *b* = 11.6676 *c* = 8.1853	6.39	1.439

Table S3. Lattice parameters of S1, S2, and S3 without and with the electric field of 400 kV cm^{-1}.

Samples	Lattice parameters under 0 kV cm^{-1}	Lattice parameters under 400 kV cm^{-1}	Increase of lattice volume (%)	Electrostrain (%)
S1	a = 4.1257 Å b = 4.1257 Å c = 4.1007 Å V = 69.80 Å^3	a = 4.1291 Å b = 4.1291 Å c = 4.1073 Å V = 70.03 Å^3	0.33	0.19
S2	a = 5.8240 Å b = 11.7272 Å c = 8.1833 Å V = 558.91 Å^3	a = 5.83336 Å b = 11.7407 Å c = 8.2041 Å V = 561.88 Å^3	0.53	0.31
S3	a = 5.8126 Å b = 11.6550 Å c = 8.1682 Å V = 553.36 Å^3	a = 5.8160 Å b = 11.6716 Å c = 8.1718 Å V = 554.72 Å^3	0.25	0.11

Table S4. Electrostrain of typical ferroelectric and antiferroelectric ceramics.

Ferroelectric/ Antiferroelectric	Lead-free/ Lead-based	Composition	Strain (%)	Ref.
Ferroelectric	Lead-free	$0.96(Na_{0.49}K_{0.49}Li_{0.02})(Nb_{0.8}Ta_{0.2})O_3$-$0.04CaZrO_3$ (KNN-CZ4)	0.17	[52]
		$(K_{0.44}Na_{0.52}Li_{0.04})(Nb_{0.86}Ta_{0.10}Sb_{0.04})O_3$ (KNN-LF4T)	0.15	[19]
		$0.92(Na_{0.5}K_{0.5})NbO_3$-$0.02(Bi_{0.5}Li_{0.5})TiO_3$-$0.06BaZrO_3$+1.5 wt% MnO_2 (KNN-BLT-BZ-Mn)	0.18	[53]
		$0.67Bi_{1.05}FeO_3$-$0.33BaTiO_3$ (67BF-33BT)	0.21	[54]
		$(Na_{1/2}Bi_{1/2})_{0.935}Ba_{0.065}Ti_{0.975}(Fe_{1/2}Nb_{1/2})_{0.025}O_3$ (NBT-BT-0.025FN)	0.39	[55]
		$0.65BiFeO_3$-$0.3BaTiO_3$-$0.05Bi(Zn_{2/3}Nb_{1/3})O_3$+0.1 wt % Mn_2O_3 (BF-BT-0.05BZN)	0.46	[56]
		$Ag_{0.94}K_{0.06}NbO_3$ (AKN0.06)	0.40	[57]
	Lead-based	$0.925[0.73Pb(Mg_{1/3}Nb_{2/3})O_3$-$0.27PbTiO_3]$-$0.075Bi(Zn_{1/2}Ti_{1/2})O_3$ (PMN-PT-7.5BZT)	0.27	[58]
		$0.4PbTiO_3$-$0.57PbZrO_3$-$0.03(La_{0.1}Sr_{0.80.1})TiO_{2.95}$ (0.4PT-PZ-LST)	0.30	[59]
		$0.1Bi(Mg_{1/2}Ti_{1/2})O_3$-$0.6Pb(Mg_{1/3}Nb_{2/3})O_3$-$0.3PbTiO_3$ (0.1BMT-PMN-PT)	0.37	[60]
		$(Pb_{0.975}Ce_{0.025})(Mg_{1/3}Nb_{2/3})_{0.71}Ti_{0.29}O_3$ (2.5Ce-PMNT29)	0.20	[61]
Antiferroelectric		$NaNbO_3$ (NN)	0.27	[62]

	Lead-free	$0.84NaNbO_3$-$0.16SrTiO_3$ (0.84NN-0.16ST)	0.29	[63]
		$0.91NaNbO_3$-$0.06BaZrO_3$-$0.03CaZrO_3$ (0.91NN-0.06BZ-0.03CZ)	0.35	[64]
		$0.88NaNbO_3$-$0.12SrTiO_3$+0.3 wt%MnO_2 (NNST-0.3Mn)	0.33	[65]
		$0.82(0.94Bi_{0.5}Na_{0.5}TiO_3$-$0.06BaTiO_3)$-$0.18K_{0.5}Na_{0.5}NbO_3$ (BNT-BT-18KNN)	0.15	[66]
		$90Bi_{0.5}Na_{0.5}TiO_3$-$5SrTiO_3$-$5K_{0.5}Na_{0.5}NbO_3$ (BNST5KNN)	0.37	[21]
Antiferroelectric	Lead-based	$[(Pb_{0.85}Ba_{0.15})_{0.9925}La_{0.005}](Zr_{0.52}Ti_{0.48})O_3$ (PZT4)	0.13	[19]
		$(Pb_{0.92}La_{0.08})(Zr_{0.70}Ti_{0.30})_{0.98}O_3$ (PLZT)	0.23	[67]
		$Pb[(Zr_{0.57}Sn_{0.43})_{0.94}Ti_{0.06}]O_3$ (PZST)	0.21	[68]
		$(Pb_{0.99}Nb_{0.02})[(Zr_{0.52}Sn_{0.48})_{0.955}Ti_{0.045}]_{0.98}O_3$ (PNZST)	0.22	[69]
		$(Pb_{0.97}La_{0.02})(Zr_{0.85}Sn_{0.08}Ti_{0.07})O_3$ (PLZST)	0.40	[70]
		$(Pb_{0.98}La_{0.02})(Zr_{0.70}Hf_{0.30})_{0.9225}Ti_{0.0775}O_3$ (PLZHT)	0.20	[71]
		$(Pb_{0.94}La_{0.03})[Nb_{0.03}(Zr_{0.85}Sn_{0.08}Ti_{0.07})_{0.97}]O_3$ (PLNZST)	0.47	[72]
		$(Pb_{0.915}Ba_{0.04}La_{0.03})(Zr_{0.65}Sn_{0.3}Ti_{0.05})O_3$ (PBLZST)	0.26	[73]
		$(Pb_{0.9}Ba_{0.04}La_{0.04})(Zr_{0.65}Sn_{0.3}Ti_{0.05})O_3$ (PBLZST)	**0.19**	**This work**
		$(Pb_{0.95}Ba_{0.02}La_{0.02})(Zr_{0.6}Sn_{0.4})O_3$ (PBLZS)	**0.31**	**This work**
		$(Pb_{0.92}Ca_{0.06}La_{0.02})(Zr_{0.6}Sn_{0.4})_{0.995}O_3$ (PCLZS)	**0.11**	**This work**

Note of Table S4.

The electrostrain of ferroelectric and antiferroelectric ceramics originates from the electric field-induced phase transition, lattice distortion and domain switching, which can be enhanced with various methods.

Table S4 lists the strain of typical ferroelectric and antiferroelectric ceramics. For example, in $0.67Bi_{1.05}FeO_3$-$0.33BaTiO_3$ (BF-BT), with the volatilization of Bi during the high-temperature sintering process, the Bi vacancies and the Fe ions form defect dipoles and generate a large internal bias field, increasing the strain to a high level of 0.2% with a relatively low electric field[54]. Constructing a morphotropic phase boundary (MPB) consisting of ferrielectric $Pmc2_1$ and ferroelectric $Pmc2_1$ phases, domain switching and phase transition of $AgNbO_3$-$KNbO_3$ (AKN) solid solution can be easily induced with electric fields, enabling the ceramic a high strain response of 0.4% [Ref. 57]. Moreover, by enhancing the non-180° domain wall movement with the doping of $CaZrO_3$, the electrostrain of $(Na_{0.49}K_{0.49}Li_{0.02})(Nb_{0.8}Ta_{0.2})O_3$-$x$$CaZrO_3$ (KNN-CZ) can be increased from 0.11% to 0.17% [Ref. 52].

In antiferroelectric, high strain of 0.4% can be achieved in $(Pb_{0.97}La_{0.02})(Zr_{0.85}Sn_{0.08}Ti_{0.07})O_3$ (PLZST) due to the coexistence of the orthorhombic AFE (AFE_O) and the tetragonal AFE (AFE_T) phases, as the electric field could induce a complex AFE_O/AFE_T-rhombohedra FE phase transitions[70]. Besides, an ultra-high strain of 0.5% is observed in $Pb_{0.98}Nb_{0.02}[(Zr_{0.85}Sn_{0.15})_{0.97}Ti_{0.03}]_{0.98}O_3$ (PNZST) with the electric field-induced multistage phase transitions[74].

In our experiment, the high strain response of S2 could be attributed to the special multistage phase transitions, lattice deformation and domain switching behavior with electric fields. With the increase of the electric field, the AFE phase of S2 transits to the FE_I and then the FE_{II} phase at 200 kV cm^{-1} and 270 kV cm^{-1}, respectively, as implied by the two inflection points of the charge curve of the *P*-*E* loop

(Fig. S11). Furthermore, as revealed by the in-situ XRD with electric fields (Fig. S19), the lattice volume increases by 0.53%, which is significantly larger than that of S1 and S2. Moreover, as verified by the PFM (Figs. S14 and S15), the domains of S2 can be highly aligned with electric fields, the switching of which also contributes to the large strain. The special multistage phase transitions, lattice deformation and domain switching behavior enable S2 a large strain of 0.31%.

Table S5. Comparison of adhesion strength of the cofired interface between various Ag-Pd alloy electrodes and materials.

Electrode	Material	Adhesion strength (MPa)	Ref.
Pure 70Ag-30Pd	$Pb(Mg_{1/3}Nb_{2/3})O_3$-$Pb(Zn_{1/3}Nb_{2/3})O_3$-$PbTiO_3$	4.8	[22]
70Ag-30Pd+10 wt% BT	$Pb(Mg_{1/3}Nb_{2/3})O_3$-$Pb(Zn_{1/3}Nb_{2/3})O_3$-$PbTiO_3$	7.5	[22]
70Ag-30Pd+10 wt% ceramic powders	$(Pb_{0.9}Ba_{0.04}La_{0.04})(Zr_{0.65}Sn_{0.3}Ti_{0.05})O_3$ (S1)	12.2	This work
	$(Pb_{0.95}Ba_{0.02}La_{0.02})(Zr_{0.6}Sn_{0.4})O_3$ (S2)	10.9	
	$(Pb_{0.92}Ca_{0.06}La_{0.02})(Zr_{0.6}Sn_{0.4})_{0.995}O_3$ (S3)	10.7	

Table S6. Comparison of stress levels and their effects on ferroelectric and antiferroelectric materials.

Stress	Material	Influence on performance	Ref.
0.5 MPa	PZT	The electrostrain decreases from 0.05% to 0.048%	[44]
7 MPa	PZT	The piezoelectric coefficient increases from 160 to 200 pC N^{-1}	[45]
10 MPa	(Y, Nb)-doped $BaTiO_3$	Crystal lattice distortion and changes in domain structure lead to an increase in dielectric constant	[46]
40 MPa	BCZT	The polarization increases from 8.5 to 15.2 μC cm^{-2}	[47]
100 MPa	PBLZST	The antiferroelectric-ferroelectric phase transition electric field increases from 14.92 to 19.32 kV cm^{-1} and the polarization decreases from 25.54 to 18.02 μC cm^{-2}	[48]
260 MPa	BCZT	The polarization decreases from 15.9 to 11.4 μC cm^{-2}	[47]
3 GPa	$BaTiO_3$ thin film	The Curie temperature significantly increases to 500 ℃	[50]

Table S7. Detailed information on the lead-based materials for the energy storage performance comparison (Fig. S30).

	Composition	E_b (kV cm^{-1})	W_{rec} (J cm^{-3})	η (%)	Ref.
Bulk ceramic	$(Pb_{0.94}La_{0.04})[(Zr_{0.70}Sn_{0.30})_{0.90}Ti_{0.10}]O_3$ (PLZST)	104	1.39	92	[75]
	$(Pb_{0.94}La_{0.04})[(Zr_{0.6}Sn_{0.4})_{0.92}Ti_{0.08}]O_3$ (PLZST)	327	5.2	91.2	[76]
	$(Pb_{0.955}La_{0.03})(Zr_{0.50}Sn_{0.42}Ti_{0.08})O_3$ (PLZST)	180	3.99	79.2	[77]
	$(Pb_{0.955}Sr_{0.015}La_{0.02})(Zr_{0.75}Sn_{0.195}Ti_{0.055})O_3$ (PSLZST)	330	5.56	67.9	[78]
	$(Pb_{0.955}Cd_{0.015}La_{0.02})(Zr_{0.50}Sn_{0.45}Ti_{0.05})O_3$ (PCLZST)	290	6.48	87.1	[79]
	$(Pb_{0.915}Ba_{0.04}La_{0.03})(Zr_{0.65}Sn_{0.3}Ti_{0.05})O_3$ (PBLZST)	170	4.44	88.8	[73]
	$(Pb_{0.87}Ba_{0.1}La_{0.02})(Zr_{0.65}Sn_{0.3}Ti_{0.05})O_3$-0.0075Y (PBLYZST)	130	2.75	71.5	[80]
	$[Pb_{0.81}La_{0.02}(Li_{1/2}Bi_{1/2})_{0.12}Sr_{0.04}](Zr_{0.57}Sn_{0.34}Ti_{0.09})O_3$ (PLLBSZST)	210	3.22	94	[81]
	$(Pb_{0.98}La_{0.02})(Zr_{0.55}Sn_{0.45})_{0.995}O_3$ (PLZS)	350	8.3	87.6	[82]
	$(Pb_{0.97}Sr_{0.03})(Zr_{0.5}Sn_{0.5})O_3$ (PSZS)	390	10.5	83.3	[83]
	$(Pb_{0.95}Ca_{0.02}La_{0.02})(Zr_{0.6}Sn_{0.4})O_3$ (PCLZS)	460	10.04	83.95	[84]
	$(Pb_{0.94}La_{0.04})(Zr_{0.65}Sn_{0.35})_{0.975}Nb_{0.02}O_3$ (PLZSN)	400	8.26	90.31	[85]
	$(Pb_{0.91}Ba_{0.045}La_{0.03})(Zr_{0.6}Sn_{0.4})O_3$ (PBLZS)	340	8.16	92.1	[86]
	$(Pb_{0.95}Ba_{0.02}La_{0.02})(Zr_{0.6}Sn_{0.4})O_3$ (PBLZS)	450	12.8	84.2	[87]
	$(Pb_{0.9}Ba_{0.04}Sr_{0.04}La_{0.02})(Zr_{0.45}Sn_{0.55})_{0.995}O_3$ (PBSLZS)	350	7.01	89.9	[88]

$(Pb_{0.91}La_{0.06})(Zr_{0.552}Sn_{0.368}Ti_{0.08})O_3$@1wt%$PbO-B_2O_3-SiO_2-Al_2O_3-ZnO-MnO_2$ (PLZST@PBSAZM)	380	7.4	91.6	[89]
$(Pb_{0.97}La_{0.02})(Zr_{0.33}Sn_{0.55}Ti_{0.12})O_3$@0.05$SiO_2$ (PLZST@SiO_2)	238	2.68	83	[90]
$Pb_{0.95}La_{0.02}Sr_{0.02}(Zr_{0.50}Sn_{0.40}Ti_{0.10})O_3$-0.8 wt% Al_2O_3 (PLSZST-Al_2O_3)	220	3.23	90	[91]
$(Pb_{0.915}Ba_{0.04}La_{0.03})(Zr_{0.65}Sn_{0.3}Ti_{0.05})O_3$-1.0 wt% AlN (PBLZST-AlN)	290	5.6	88.1	[92]
$(Pb_{0.93}Ba_{0.04}La_{0.02})(Zr_{0.65}Sn_{0.3}Ti_{0.05})O_3$-0.1 wt% MgO (PBLZST-MgO)	246	5.02	76.8	[93]
0.7$(Pb_{0.9}Ba_{0.04}La_{0.04})(Zr_{0.65}Sn_{0.3}Ti_{0.05})O_3-0.3(Pb_{0.955}La_{0.03})(Zr_{0.80}Sn_{0.19}Ti_{0.01})O_3$ (PBLZST-PLZST)	470	9.8	87.5	[94]
0.99$(Pb_{0.97}La_{0.02})(Zr_{0.6}Sn_{0.4})O_3-0.01AgNbO_3$ (PLZS-AN)	400	10.81	85.05	[95]
$(Pb_{0.91}Ba_{0.015}La_{0.05})(Zr_{0.6}Sn_{0.4})O_3$-0.4wt%$BaO-B_2O_3-Al_2O_3-SiO_2$ (PBLZS-BBAS)	390	6.3	87	[96]
$PbHfO_3$ (PH)	270	7.6	80.8	[97]
$Pb_{1.045}HfO_3$ (PH)	250	7.29	73.18	[98]
0.95$PbHfO_3$-0.05$Pb(Zn_{1/2}W_{1/2})O_3$ (PH-PZW)	200	5.03	60	[99]
$(Pb_{0.96}La_{0.04})(Zr_{0.99}Ti_{0.01})O_3$ (PLZT)	395	11.38	79	[100]
$(Pb_{0.97}La_{0.02})(Zr_{0.93}Sn_{0.05}Ti_{0.02})O_3$ (PLZST)	376	12.1	75.2	[6]
$(Pb_{0.98}La_{0.02})(Zr_{0.55}Sn_{0.43}Ti_{0.02})_{0.995}O_3$ (PLZST)	290	5.7	83	[101]
$(Pb_{0.94}La_{0.04})(Zr_{0.99}Sn_0Ti_{0.01})O_3$ (PLZST)	400	13	78.1	[102]
$(Pb_{0.94}La_{0.04})(Zr_{0.49}Sn_{0.5}Ti_{0.01})O_3$ (PLZST)	400	9.6	90.2	[5]
$(Pb_{0.95}Ca_{0.02}La_{0.02})(Zr_{0.93}Sn_{0.05}Ti_{0.02})O_3$ (PCLZST)	448	14.5	77.1	[103]

Thick film	$(Pb_{0.97}La_{0.02}Ca_{0.01})(Zr_{0.6}Sn_{0.4})_{0.97}Ta_{0.02}O_3$ (PLCZST)	300	7.93	93.9	[104]
	$(Pb_{0.91}La_{0.04}Ca_{0.03})[Nb_{0.02}(Zr_{0.99}Ti_{0.01})_{0.975}]O_3$ (PLCNZT)	420	12.15	85.4	[105]
	$(Pb_{0.97}Gd_{0.02})(Zr_{0.87}Sn_{0.12}Ti_{0.01})O_3$ (PGZST)	447	12	78	[106]
	$(Pb_{0.97}La_{0.02})(Zr_{0.85}Sn_{0.12}Ti_{0.03})O_3$@0.5wt%$Al_2O_3$ (PLZST@Al_2O_3)	315	5.3	88.3	[107]
	$(Pb_{0.98}La_{0.02})(Zr_{0.45}Sn_{0.55})_{0.995}O_3$ (PLZS)	400	7.09	88	[108]
	$(Pb_{0.98}La_{0.02})(Zr_{0.55}Sn_{0.45})_{0.995}O_3$ (PLZS)	400	10.4	87	[9]
	$(Pb_{0.94}La_{0.02}Sr_{0.04})(Zr_{0.9}Sn_{0.1})_{0.995}O_3$ (PLSZS)	395	11.18	82.2	[109]
	$(Pb_{0.88}Cd_{0.03}La_{0.06})(Zr_{0.6}Sn_{0.4})O_3$ (PCLZS)	870	19.3	91	[110]
	$(Pb_{0.925}Ba_{0.045}La_{0.03})(Hf_{0.6}Sn_{0.4})_{0.9925}O_3$ (PBLHS)	290	7.3	91	[111]
	$(Pb_{0.97}La_{0.02})HfO_3$ (PLHT)	300	7.1	78.5	[112]
	$(Pb_{0.98}La_{0.02})(Hf_{0.45}Sn_{0.55})_{0.995}O_3$ (PLHS)	380	7.63	94	[113]
Multilayer ceramic capacitor	PLZT	680	12.4	90	[114]
	$(Pb_{0.98}La_{0.02})(Zr_{0.7}Sn_{0.3})_{0.995}O_3$ (PLZS)	560	12.6	80	[115]
	$(Pb_{0.92}La_{0.02}Ca_{0.06})(Zr_{0.6}Sn_{0.4})_{0.995}O_3$ (PLCZS)	760	15.9	92	[51]
	$(Pb_{0.94}La_{0.02}Ca_{0.04})(Zr_{0.7}Sn_{0.3})_{0.995}O_3$ (PLCZS)	530	14.3	86.1	[116]
	$Pb_{0.9}Ba_{0.04}La_{0.04})(Zr_{0.65}Sn_{0.3}Ti_{0.05})O_3$/$(Pb_{0.95}Ba_{0.02}La_{0.02})(Zr_{0.6}Sn_{0.4})O_3$/ $(Pb_{0.92}Ca_{0.06}La_{0.02})(Zr_{0.6}Sn_{0.4})_{0.995}O_3$ (PBLZST/PBLZS/PCLZS)	**750**	**22.0**	**96.1**	**This work**

Table S8. Detailed information on the MLCCs for the energy storage performance comparison (Fig. 5c).

	Composition	Internal electrode	E_b (kV cm^{-1})	W_{rec} (J cm^{-3})	η (%)	Ref.
Lead-based	PLZT	-	680	12.4	90	[114]
	$(Pb_{0.98}La_{0.02})(Zr_{0.7}Sn_{0.3})_{0.995}O_3$ (PLZS)	Pt	355	12.6	80	[115]
	$(Pb_{0.92}La_{0.02}Ca_{0.06})(Zr_{0.6}Sn_{0.4})_{0.995}O_3$ (PLCZS)	Pt	760	15.9	92	[51]
	$(Pb_{0.94}La_{0.02}Ca_{0.04})(Zr_{0.7}Sn_{0.3})_{0.995}O_3$ (PLCZS)	Pt	530	14.3	86.1	[116]
$BaTiO_3$-based	$0.87BaTiO_3$-$0.13Bi(Zn_{2/3}(Nb_{0.85}Ta_{0.15})_{1/3})O_3$ (BTBZNT)	Pt	1500	14.08	69.7	[117]
	$0.87BaTiO_3$-$0.13Bi(Zn_{2/3}(Nb_{0.85}Ta_{0.15})_{1/3})O_3$ (BTBZNT)	60Ag-40Pd	1000	10.5	93.7	[118]
	$0.87BaTiO_3$-$0.13Bi(Zn_{2/3}(Nb_{0.85}Ta_{0.15})_{1/3})O_3$ (BTBZNT)	60Ag-40Pd	750	8.13	95	[119]
	$0.87BaTiO_3$-$0.13Bi(Zn_{2/3}(Nb_{0.85}Ta_{0.15})_{1/3})O_3$ (BTBZNT)	60Ag-40Pd	1047	10.12	89.4	[120]
	$0.87BaTiO_3$-$0.13Bi(Zn_{2/3}(Nb_{0.85}Ta_{0.15})_{1/3})O_3$ (BTBZNT)	60Ag-40Pd	790	7.8	88	[121]
	$0.9BaTiO_3$-$0.1Bi(Li_{0.5}Nb_{0.5})O_3$ (BT-BLN)	Pt	450	4.5	91.5	[122]
	$0.9BaTiO_3$-$0.1Bi(Li_{0.5}Ta_{0.5})O_3$ (BT-BLT)	Pt	466	4.05	95.5	[123]
	$(Ba_{0.33}Bi_{0.32}Ca_{0.11}Sm_{0.07}Na_{0.07}Sr_{0.1})(Ti_{0.63}Fe_{0.32}Zr_{0.05})O_3$ (BBCSNSTFZ)	70Ag-30Pd	1094	20.8	97.5	[124]
	$0.65(Na_{0.5}Bi_{0.5})TiO_3$-$0.35(Sr_{0.7}Bi_{0.2})TiO_3$ (NBT-SBT)	Pt	1030	21.5	80	[125]

$Bi_{0.5}Na_{0.5}TiO_3$-based	$0.62Na_{0.5}Bi_{0.5}TiO_3$-$0.3Sr_{0.7}Bi_{0.2}TiO_3$-$0.08BiMg_{2/3}Nb_{1/3}O_3$ (NBT-SBT-BMN)	Pt	1013	18	93	[126]
	$0.85(0.65Bi_{0.5}Na_{0.5}TiO_3$-$0.35SrTiO_3)$-$0.15La(Mg_{1/2}Zr_{1/2})O_3$ (NBT-ST-LMZ)	Pt	1050	13.5	90	[127]
	$0.55(Na_{0.5}Bi_{0.5})TiO_3$-$0.45(Sr_{0.7}Bi_{0.2})TiO_3$ (NBT-SBT)	Pt	720	9.5	92	[128]
	$0.6Bi_{0.5}Na_{0.5}TiO_3$-$0.4SrTiO_3$ (BNT-ST)	75Ag-25Pd	270	2.83	85	[129]
	$Na_{0.5}Bi_{0.5}TiO_3$-$0.50Sr_{0.85}Bi_{0.10}TiO_3$ (NBT-SBT)	Pt	420	4.9	72	[130]
$BiFeO_3$-based	$0.65BiFeO_3$-$0.3BaTiO_3$-$0.05NaTaO_3$ + 0.3 wt% MnO_2 (BF-BT-NT)	Pt	780	9.1	80	[131]
	$0.5BiFeO_3$-$0.4SrTiO_3$-$0.03Nb_2O_5$-$0.1BiMg_{2/3}Nb_{1/3}O_3$ (BF-ST-Nb-BMN)	Pt	1000	15.8	75.2	[132]
	$0.57BiFeO_3$-$0.30BaTiO_3$-$0.13Bi(Li_{0.5}Nb_{0.5})O_3$ (BF-BT-BLN)	Pt	953	13.8	81	[133]
	$0.62BiFeO_3$-$0.3BaTiO_3$-$0.08Nd(Zr_{0.5}Zn_{0.5})O_3$ (BF-BT-NZZ)	Pt	700	10.5	87	[134]
	$0.61BiFeO_3$-$0.33(Ba_{0.8}Sr_{0.2})TiO_3$-$0.06La(Mg_{2/3}Nb_{1/3})O_3$ (BF-BST-LMN)	Pt	730	10	72	[135]
	$0.75(Bi1_{0.85}Nd_{0.15})FeO_3$-$0.25BaTiO_3$ (BNF-BT)	Pt	540	6.74	77	[136]
$AgNbO_3$-based	$Sm_{0.05}Ag_{0.85}Nb_{0.7}Ta_{0.3}O_3$ (SANT)	Pt	1450	14	85	[7]
	$Ag(Nb_{0.85}Ta_{0.15})O_3$ + 0.25 wt% MnO_2 (ANT-Mn)	Pt	1020	7.9	71	[137]
$NaNbO_3$-based	$0.67NaNbO_3$-$0.18(Bi_{0.5}Na_{0.5})TiO_3$-$0.15Bi(Mg_{0.5}Hf_{0.5})O_3$ (NN-BNT-BMH)	70Ag-30Pd	1100	12.65	88.5	[138]
	$0.80NaNbO_3$-$0.04CaZrO_3$-$0.16Bi_{0.5}Na_{0.5}TiO_3$ (NN-CZ-BNT)	Pt	400	3.7	82.1	[139]
Lead-based	**$(Pb_{0.9}Ba_{0.04}La_{0.04})(Zr_{0.65}Sn_{0.3}Ti_{0.05})O_3$/$(Pb_{0.95}Ba_{0.02}La_{0.02})(Zr_{0.6}Sn_{0.4})O_3$/ $(Pb_{0.92}Ca_{0.06}La_{0.02})(Zr_{0.6}Sn_{0.4})_{0.995}O_3$ (PBLZST/PBLZS/PCLZS)**	**70Ag-30Pd**	**750**	**22.0**	**96.1**	**This work**

Supplementary References

1. Palneedi, H., Peddigari, M., Hwang, G. T., Jeong, D. Y. & Ryu, J. High-performance dielectric ceramic films for energy storage capacitors: progress and outlook. *Adv. Funct. Mater.* **28**, 1803665 (2018).
2. Zheng, J., Takahashi, S., Yoshikawa, S., Uchino, K. & de Vries, J. W. C. Heat generation in multilayer piezoelectric actuators. *J. Am. Ceram. Soc.* **79**, 3193-3198 (2005).
3. Levesque, L. Law of cooling, heat conduction and Stefan-Boltzmann radiation laws fitted to experimental data for bones irradiated by CO_2 laser. *Biomed. Opt. Express* **5**, 701-712 (2014).
4. Fu, D. et al. Piezoelectric properties of lithium modified silver niobate perovskite single crystals. *Appl. Phys. Lett.* **92** (2008).
5. Meng, X., Zhao, Y., Li, Y. & Hao, X. Systematical investigation on energy-storage behavior of PLZST antiferroelectric ceramics by composition optimizing. *J. Am. Ceram. Soc.* **104**, 2170-2180 (2021).
6. Zhang, Y. et al. Achieving excellent energy storage density of $Pb_{0.97}La_{0.02}(Zr_xSn_{0.05}Ti_{0.95-x})O_3$ ceramics by the B-site modification. *J. Eur. Ceram. Soc.* **41**, 360-367 (2021).
7. Zhu, L. F. et al. Heterovalent-doping-enabled atom-displacement fluctuation leads to ultrahigh energy-storage density in $AgNbO_3$-based multilayer capacitors. *Nat. Commun.* **14**, 1166 (2023).
8. Li, S. et al. Giant energy density and high efficiency achieved in silver niobate-based lead-free antiferroelectric ceramic capacitors via domain engineering. *Energy Storage Mater.* **34**, 417-426 (2021).
9. Wang, H., Liu, Y., Yang, T. & Zhang, S. Ultrahigh energy-storage density in antiferroelectric ceramics with field-induced multiphase transitions. *Adv. Funct. Mater.* **29**, 1807321 (2019).
10. Gao, L., Guo, H., Zhang, S. & Randall, C. A. Stabilized antiferroelectricity in $x$$BiScO_3$-$(1-x)$$NaNbO_3$ lead-free ceramics with established double hysteresis loops. *Appl. Phys. Lett.* **112**, 092905 (2018).
11. Gao, L., Guo, H., Zhang, S. & Randall, C. A. A perovskite lead-free antiferroelectric $x$$CaHfO_3$-$(1-x)$$NaNbO_3$ with induced double hysteresis loops at room temperature. *J. Appl. Phys.* **120**, 204102 (2016).
12. Xie, A., Qi, H. & Zuo, R. Achieving remarkable amplification of energy-storage density in two-step sintered $NaNbO_3$-$SrTiO_3$ antiferroelectric capacitors through dual adjustment of local

heterogeneity and grain scale. *ACS Appl. Mater. Interfaces* **12**, 19467-19475 (2020).

13. Qi, H. et al. Ultrahigh energy-storage density in $NaNbO_3$-based lead-free relaxor antiferroelectric ceramics with nanoscale domains. *Adv. Funct. Mater.* **29**, 1903877 (2019).
14. Qi, H. & Zuo, R. Linear-like lead-free relaxor antiferroelectric $(Bi_{0.5}Na_{0.5})TiO_3$-$NaNbO_3$ with giant energy-storage density/efficiency and super stability against temperature and frequency. *J. Mater. Chem. A* **7**, 3971-3978 (2019).
15. Toby, B. H. EXPGUI, a graphical user interface for GSAS. *J. Appl. Cryst.* **34**, 210-213 (2001)
16. Toby, B. H. R factors in Rietveld analysis: How good is good enough? *Powder Diffr.* **21**, 67-70 (2012).
17. Huan, Y. et al. Achieving excellent energy storage reliability and endurance via mechanical performance optimization strategy in engineered ceramics with core-shell grain structure. *J. Materiomics* **8**, 601-610 (2022).
18. Tomer, V., Manias, E. & Randall, C. A. High field properties and energy storage in nanocomposite dielectrics of poly(vinylidene fluoride-hexafluoropropylene). *J. Appl. Phys.* **110**, 044107 (2011).
19. Saito, Y. et al. Lead-free piezoceramics. *Nature* **432**, 84-87 (2004).
20. Ge, J. et al. Enhancement of energy storage in epitaxial $PbZrO_3$ antiferroelectric films using strain engineering. *Appl. Phys. Lett.* **105**, 112908 (2014).
21. Liu, L. et al. Large strain response based on relaxor-antiferroelectric coherence in $Bi_{0.5}Na_{0.5}TiO_3$-$SrTiO_3$-$(K_{0.5}Na_{0.5})NbO_3$ solid solutions. *J. Appl. Phys.* **116**, 184104 (2014).
22. Zuo, R., Li, L., Gui, Z., Hu, X. & Ji, C. Effects of additives on the interfacial microstructure of cofired electrode-ceramic multilayer systems. *J. Am. Ceram. Soc.* **85**, 787-793 (2004).
23. Wang, S. F., Dougherty, J. P., Huebner, W. & Pepin, J. G. Silver-palladium thick-film conductors. *J. Am. Ceram. Soc.* **77**, 3051-3072 (2005).
24. Kojima, S. Poisson's ratio of glasses, ceramics, and crystals. *Materials* **17**, 300 (2024).
25. Small, M. K., Daniels, B. J., Clemens, B. M., & Nix, W. D. The elastic biaxial modulus of Ag-Pd multilayered thin films measured using the bulge test. *J. Mater. Res.* **9**, 25-30 (1994).
26. Wang, D. et al. Von Mises Stress in Chemical - Mechanical Polishing Processes. *J. Electrochem. Soc.* **144**, 1121-1127 (2019).
27. Yang, Z. et al. Residual stress characterization in microelectronic manufacturing: An analysis based on Raman spectroscopy. *Laser Photonics Rev.* **18**, 2301300 (2024).

28. Deluca, M., & Pezzotti, G. First-order transverse phonon deformation potentials of tetragonal perovskites. *J. Phys. Chem. A* **112**, 11165-11171 (2008).
29. Ding, M., He, X., Cheng, X., Zhang, Y. & Yang, F. An in-situ Raman spectroscopic investigation of PLZT ceramic under a coupled mechanical-electrical load. *J. Electroceram.* **46**, 162-171 (2021).
30. Deluca, M., Sakashita, T., Galassi, C. & Pezzotti, G. Investigation of local orientation and stress analysis of PZT-based materials using micro-probe polarized Raman spectroscopy. *J. Eur. Ceram. Soc.* **26**, 2337-2344 (2006).
31. Deluca, M., Sakashita, T., Zhu, W., Chazono, H. & Pezzotti, G. Stress dependence of the polarized Raman spectrum of polycrystalline lead zirconate titanate. *J. Appl. Phys.* **101**, 083526 (2007).
32. Tan, X. et al. Electric-field-induced antiferroelectric to ferroelectric phase transition in mechanically confined $Pb_{0.99}Nb_{0.02}[(Zr_{0.57}Sn_{0.43})_{0.94}Ti_{0.06}]_{0.98}O_3$. *Phys. Rev. B* **81**, 014103 (2010).
33. Peláiz-Barranco, A., & Hall, D. A. Influence of composition and pressure on the electric field-induced antiferroelectric to ferroelectric phase transformation in lanthanum modified lead zirconate titanate ceramics. *Ieee T. Ultrason. Ferr.* **56**, 1785-1791 (2009).
34. Xu, Y. et al. Effect of Ba content on the stress sensitivity of the antiferroelectric to ferroelectric phase transition in (Pb,La,Ba,)(Zr,Sn,Ti)O_3 ceramics. *J. Am. Ceram. Soc.* **97**, 206-212 (2013).
35. Hyun, S. & Char, K. Effects of strain on the dielectric properties of tunable dielectric $SrTiO_3$ thin films. *Appl. Phys. Lett.* **79**, 254-256 (2001).
36. Taylor, T. R. et al. Impact of thermal strain on the dielectric constant of sputtered barium strontium titanate thin films. *Appl. Phys. Lett.* **80**, 1978-1980 (2002).
37. Canedy, C. L. et al. Dielectric properties in heteroepitaxial $Ba_{0.6}Sr_{0.4}TiO_3$ thin films: Effect of internal stresses and dislocation-type defects. *Appl. Phys. Lett.* **77**, 1695-1697 (2000).
38. Shin, H., Park, J.-S., Kim, S., Jung, H. S. & Hong, K. S. Investigation of useful or deleterious residual thermal stress component to the capacitance of a multilayer ceramic capacitor. *Microelectron. Eng.* **77**, 270-276 (2005).
39. Sugimura, K. I., & Hirao, K. Effect of a $BaTiO_3$ nanoparticle additive on the quality of thin-film Ni electrodes in MLCC. *J. Ceram. Soc. Jpn.* **117**, 1039-1043 (2009).
40. Lee, Y.-C. & Chiang, C.-S. High dielectric constant of $(Ba_{0.96}Ca_{0.04})(Ti_{0.85}Zr_{0.15})O_3$ multilayer ceramic capacitors with Cu doped Ni electrodes. *J. Alloy. Compd.* **509**, 6973-6979 (2011).
41. Luo, Z. et al. Bilayer-structured nanocomposites with ultrahigh energy density and large discharge

efficiency at high temperature via balancing energy storage and thermal conductive layers. *Mater. Today Energy* **33**, 101277 (2023).

42. Taherkhani, F. & Fortunelli, A. Chemical ordering and temperature effects on the thermal conductivity of Ag-Au and Ag-Pd bimetallic bulk and nanocluster systems. *New J. Chem.* **46**, 19213-19229 (2022).
43. Zuo, R., Li, L., Hu, X., & Gui, Z. Improvement of Ag-Pd alloy electrode by ceramic dopant applied for multilayer electronic ceramic devices. *Mater. Lett.* **51**, 504-508 (2001).
44. Zhang, Q. M., & Zhao, J. Electromechanical properties of lead zirconate titanate piezoceramics under the influence of mechanical stresses. *IEEE Trans. Ultrason. Ferroelectr. Freq. Control* **46**, 1518-1526 (1999).
45. Hall, D. A. Review nonlinearity in piezoelectric ceramics. *J. Mater. Sci.* **36**, 4575-4601 (2001).
46. Yang, G., Yue, Z., Gui, Z. & Li, L. Dielectric responses of modified $BaTiO_3$ ceramics in multilayer ceramic capacitors to the combined uniaxial stress and dc bias field. *J. Appl. Phys.* **104**, 074115 (2008).
47. Maier, J. G., Gadelmawla, A., Khansur, N. H. & Webber, K. G. Stress-induced tailoring of energy storage properties in lead-free $Ba_{0.85}Ca_{0.15}Zr_{0.1}Ti_{0.9}O_3$ ferroelectric bulk ceramics. *J. Materiomics* **9**, 673-682 (2023).
48. Xu, Y., Feng, Y., Zhang, N., Yan, Y. & Liao, L. Phenomenological theory of electric-field-induced phase transition behavior of antiferroelectric ceramic $(Pb,Ba,La)(Zr,Sn,Ti)O_3$ under uniaxial compressive pre-stress. *J. Appl. Phys.* **112**, 034112 (2012).
49. Martin, L. W. & Rappe, A. M. Thin-film ferroelectric materials and their applications. *Nat. Rev. Mater.* **2**, 1-14 (2016).
50. Choi, K. J. et al. Enhancement of ferroelectricity in strained $BaTiO_3$ thin films. *Science* **306**, 1005-1009 (2004).
51. Zhao, Y., Meng, X. & Hao, X. Synergistically achieving ultrahigh energy-storage density and efficiency in linear-like lead-based multilayer ceramic capacitor. *Scripta Mater.* **195**, 113723 (2021).
52. Zhang, M.-H. et al. Enhanced electric-field-induced strains in $(K,Na)NbO_3$ piezoelectrics from heterogeneous structures. *Mater. Today* **46**, 44-53 (2021).
53. Zhang, M. H. et al. High and temperature-insensitive piezoelectric strain in alkali niobate lead-free

perovskite. *J. Am. Chem. Soc.* **139**, 3889-3895 (2017).

54. Lin, J. et al. Ultrahigh piezoelectric response obtained by artificially generating a large internal bias field in $BiFeO_3$-$BaTiO_3$ lead-free ceramics. *Adv. Funct. Mater.* **34**, 2313879 (2024).
55. Liu, K. et al. Large electrostrain in low-temperature sintered NBT-BT-0.025FN incipient piezoceramics. *J. Am. Ceram. Soc.* **103**, 3739-3747 (2020).
56. Wang, D. et al. High energy storage density and large strain in $Bi(Zn_{2/3}Nb_{1/3})O_3$-doped $BiFeO_3$-$BaTiO_3$ ceramics. *ACS Applied Energy Materials* **1**, 4403-4412 (2018).
57. Tian, Y. et al. Morphotropic phase boundary, polymorphic phases and enhanced electrostrain/piezoelectricity in $Ag_{1-x}K_xNbO_3$ solid-solution ceramics. *J. Eur. Ceram. Soc.* **43**, 4395-4407 (2023).
58. Xia, X. et al. Critical state to achieve a giant electric field-induced strain with a low hysteresis in relaxor piezoelectric ceramics. *J. Materiomics* **7**, 1143-1152 (2021).
59. Liu, J. et al. Achieving large strain and excellent temperature stability in PT-PZ-LST piezoelectric ceramics. *Ceram. Int.* **50**, 6870-6879 (2024).
60. Jia, H., Liang, Z., Li, Z., Li, F. & Wang, L. Texture technique to simultaneously achieve large electric field induced strain response and ultralow hysteresis in BMT-PMN-PT relaxor ferroelectric ceramics. *Scripta Mater.* **209**, 114409 (2022).
61. Huang, Y. et al. Boosting piezoelectric response and electric-field induced strain in PMN-PT relaxor ferroelectrics. *J. Eur. Ceram. Soc.* **44**, 7572-7581 (2024).
62. Zhang, M.-H. et al. Revealing the mechanism of electric-field-induced phase transition in antiferroelectric $NaNbO_3$ by in situ high-energy X-ray diffraction. *Appl. Phys. Lett.* **118**, 132903 (2021).
63. Xie, A. et al. An environmentally-benign $NaNbO_3$ based perovskite antiferroelectric alternative to traditional lead-based counterparts. *J. Mater. Chem. C* **7**, 15153-15161 (2019).
64. Zuo, R., Fu, J. & Qi, H. Stable antiferroelectricity with incompletely reversible phase transition and low volume-strain contribution in $BaZrO_3$ and $CaZrO_3$ substituted $NaNbO_3$ ceramics. *Acta Mater.* **161**, 352-359 (2018).
65. Xie, A., Liu, L., Zhang, Y., Rahman, A. & Zuo, R. MnO_2 doping stabilized antiferroelectric p phase and underlying physical mechanism in $NaNbO_3$-$SrTiO_3$ lead-free ceramics. *J. Eur. Ceram. Soc.* **44**, 882-890 (2024).

66. Zhang, S. T. et al. High-strain lead-free antiferroelectric electrostrictors. *Adv. Mater.* **21**, 4716-4720 (2009).

67. Gözüaçık, N. K., Mensur-Alkoy, E. & Alkoy, S. Effects of lanthanum doping on electrical and electromechanical properties of $(Pb_{1-x}La_x)(Zr_{0.70}Ti_{0.30})O_3$ ceramics. *J. Mater. Sci.-Mater. El.* **30**, 14045-14052 (2019).

68. Sarı, H. A., Gözüaçık, N. K., Kaya, M. Y., Menşur, E. & Alkoy, S. Lead-based antiferroelectrics revisited for high energy density capacitors and large strain actuators. *Ferroelectrics* **586**, 21-40 (2022).

69. Lyu, C. et al. Tem study of incommensurate superstructure in $Pb_{1-0.5x}Nb_x[(Zr_{0.52}Sn_{0.48})_{0.955}Ti_{0.045}]_{1-x}O_3$ ceramics with 0-1 switching characteristic strain and high energy storage density. *J. Mater. Sci.-Mater. El.* **30**, 12375-12381 (2019).

70. Ji, Y. et al. Reversible and high-temperature-stabilized strain in $(Pb,La)(Zr,Sn,Ti)O_3$ antiferroelectric ceramics. *ACS Appl. Mater. Interfaces* **11**, 32135-32143 (2019).

71. Heremans, C. & Tuller, H. L. Field-induced antiferroelectric–ferroelectric phase transitions in the $Pb_{0.98}La_{0.02}(Zr_{0.70}Hf_{0.30})_{1-x}Ti_xO_3$ system. *J. Appl. Phys.* **87**, 1458-1466 (2000).

72. Hu, J. et al. Achieving low field-induced large strain by La-Nb co-doping in PZST-based anti-ferroelectric ceramics for high-performance actuators. *J. Eur. Ceram. Soc.* **44**, 1554-1561 (2024).

73. Yang, Y. et al. Low electric-field-induced strain and high energy storage efficiency in $(Pb,Ba,La)(Zr,Sn,Ti)O_3$ antiferroelectric ceramics through regulating the content of La. *Ceram. Int.* **46**, 18106-18113 (2020).

74. Forst, D., Li, J.-F. & Viehland, D. Observation of multiple electrically induced phase transitions and a decoupling of the induced strain and polarization in Sn-modified lead zirconate titanate. *Appl. Phys. Lett.* **71**, 1472-1474 (1997).

75. Xu, R. et al. $Pb_{0.94}La_{0.04}[(Zr_{0.70}Sn_{0.30})_{0.90}Ti_{0.10}]O_3$ antiferroelectric bulk ceramics for pulsed capacitors with high energy and power density. *Appl. Phys. Lett.* **110**, 142904 (2017).

76. Xu, R., Zhu, Q., Xu, Z., Feng, Y. & Wei, X. PLZST antiferroelectric ceramics with promising energy storage and discharge performance for high power applications. *J. Am. Ceram. Soc.* **103**, 1831-1838 (2019).

77. Yu, Y. et al. High energy density and efficiency in $(Pb,La)(Zr,Sn,Ti)O_3$ antiferroelectric ceramics

with high La^{3+} content and optimized Sn^{4+} content. *Ceram. Int.* **45**, 24419-24424 (2019).

78. Zhang, Q. et al. High recoverable energy density over a wide temperature range in Sr modified (Pb,La)(Zr,Sn,Ti)O_3 antiferroelectric ceramics with an orthorhombic phase. *Appl. Phys. Lett.* **109**, 262901 (2016).
79. Lu, J., Yao, Z., Hao, H., Cao, M. & Liu, H. Antiferroelectric ceramic capacitors with high energy-storage densities and reduced sintering temperature. *Ceram. Int.* **50**, 1941-1946 (2024).
80. Zhang, L. et al. Y doping and grain size co-effects on the electrical energy storage performance of $(Pb_{0.87}Ba_{0.1}La_{0.02})(Zr_{0.65}Sn_{0.3}Ti_{0.05})O_3$ anti-ferroelectric ceramics. *Ceram. Int.* **40**, 5455-5460 (2014).
81. Liu, B., Gaur, A. P. S., Cui, J. & Tan, X. Substitution of Pb with $(Li_{1/2}Bi_{1/2})$ in $PbZrO_3$-based antiferroelectric ceramics. *J. Adv. Dielectr.* **14**, 2350022 (2023).
82. Liu, Y., Liu, S., Yang, T. & Wang, H. Achieving high energy storage density of PLZS antiferroelectric within a wide range of components. *J. Mater. Sci.* **56**, 6073-6082 (2021).
83. Ge, G. et al. Alkali-earth metal ion inducing multiphase transition of lanthanum-free $Pb(Zr_{0.5}Sn_{0.5})O_3$ ceramics improves the energy storage properties. *Appl. Phys. Lett.* **122**, 123903 (2023).
84. Jiang, S. et al. Delayed phase switching field and improved capacitive energy storage in Ca^{2+}-modified (Pb,La)(Zr,Sn)O_3 antiferroelectric ceramics. *Scripta Mater.* **235**, 115602 (2023).
85. Luo, Y., Chen, X., Fu, Z. & Wang, G. Tunable antiferroelectric ceramic polarization via regulating incommensurate phase and domain features. *Ceram. Int.* **49**, 31711-31717 (2023).
86. Huang, K., Ge, G., Yan, F., Shen, B. & Zhai, J. Ultralow electrical hysteresis along with high energy-storage density in lead-based antiferroelectric ceramics. *Adv. Electron. Mater.* **6**, 1901366 (2020).
87. Ge, G. et al. Synergistic optimization of antiferroelectric ceramics with superior energy storage properties via phase structure engineering. *Energy Storage Mater.* **35**, 114-121 (2021).
88. Li, Y., Gao, J. & Yang, T. Excellent energy density and efficiency in Ba and Sr co-doped (Pb,La)(Zr,Sn)O_3 antiferroelectric ceramics. *J. Phys. Chem. Solids* **172**, 111046 (2023).
89. Xie, J., Yao, M., Gao, W., Su, Z. & Yao, X. Ultrahigh breakdown strength and energy density in PLZST@PBSAZM antiferroelectric ceramics based on core-shell structure. *J. Eur. Ceram. Soc.* **39**, 1050-1056 (2019).
90. Bian, F. et al. Enhanced breakdown strength and energy density of antiferroelectric

Pb,La(Zr,Sn,Ti)O_3 ceramic by forming core-shell structure. *J. Eur. Ceram. Soc.* **38**, 3170-3176 (2018).

91. Sun, H. et al. Low temperature sintering of PLZST-based antiferroelectric ceramics with Al_2O_3 addition for energy storage applications. *J. Eur. Ceram. Soc.* **42**, 1380-1387 (2022).
92. Yang, Y. et al. Regulating local electric field to optimize the energy storage performance of antiferroelectric ceramics via a composite strategy. *J. Adv. Ceram.* **12**, 598-611 (2023).
93. Zhang, Y. et al. High energy storage density of tetragonal PBLZST antiferroelectric ceramics with enhanced dielectric breakdown strength. *Ceram. Int.* **46**, 3921-3926 (2020).
94. Yang, Y. et al. Interfacial polarization engineering enables superior energy storage performance in (Pb,La)(Zr,Sn,Ti)O_3-based antiferroelectric ceramics. *Ceram. Int.* **50**, 38314-38322 (2024).
95. Ge, G. et al. Optimizing the energy storage properties of antiferroelectric ceramics by modulating the phase structure via constructing a novel binary composite. *J. Mater. Chem. A* **9**, 11291-11299 (2021).
96. Huang, K. et al. Ameliorative energy-storage properties stemmed from the refined grains in PBLZS antiferroelectric ceramics via introducing liquid phase sintering. *J. Eur. Ceram. Soc.* **41**, 2450-2457 (2021).
97. Wei, J., Yang, T. & Wang, H. Excellent energy storage and charge-discharge performances in $PbHfO_3$ antiferroelectric ceramics. *J. Eur. Ceram. Soc.* **39**, 624-630 (2019).
98. Wan, H. et al. High strain and energy-storage density across a wide temperature range in fine $PbHfO_3$ ceramics. *Acta Mater.* **267**, 119715 (2024).
99. Wan, H. et al. Synergistic design of a new $PbHfO_3$-based antiferroelectric solid solution with high energy storage and large strain performances under low electric fields. *J. Mater. Chem. A* **11**, 25484-25496 (2023).
100. Liu, X., Li, Y., Li, Y. & Hao, X. Giant energy-storage density and thermally activated phase transition in $(Pb_{0.96}La_{0.04})(Zr_{0.99}Ti_{0.01})O_3$ antiferroelectric ceramics. *ACS Appl. Energ. Mater.* **4**, 4897-4902 (2021).
101. Liu, S., Liu, Y. & Yang, T. Tailoring switching field of phase transition for enhancing energy-storage density of PLZST antiferroelectric thick films. *J. Alloys Compd.* **861**, 158559 (2021).
102. Meng, X., Zhao, Y., Li, Y. & Hao, X. Simultaneously achieving ultrahigh energy density and power

density in $PbZrO_3$-based antiferroelectric ceramics with field-induced multistage phase transition. *J. Alloys Compd.* **868**, 159149 (2021).

103. Zhang, Y. et al. Ultrahigh energy storage density of Ca^{2+}-modified PLZST antiferroelectric ceramics prepared by the tape-casting method. *J. Eur. Ceram. Soc.* **41**, 4138-4145 (2021).
104. Zhao, H. et al. Ultrahigh power density and energy storage density of Ti-free Ca-doped (Pb,La)(Zr,Sn)TaO_3 antiferroelectric ceramics. *J. Mater. Chem. C* **11**, 12280-12285 (2023).
105. Quan, K. et al. High-performance antiferroelectric ceramics via multistage phase transition. *J. Am. Ceram. Soc.* **106**, 420-429 (2022).
106. Li, C., Yao, M. & Yao, X. An effective strategy for enhancing energy storage density in $(Pb_{1-1.5x}Gd_x)(Zr_{0.87}Sn_{0.12}Ti_{0.01})O_3$ antiferroelectric ceramics. *J. Mater. Chem. A* **11**, 18689-18701 (2023).
107. Li, C., Yao, M., Gao, W. & Yao, X. High breakdown strength and energy density in antiferroelectric PLZST ceramics with Al_2O_3 buffer. *Ceram. Int.* **46**, 722-730 (2020).
108. Wang, X., Yang, T., Shen, J. & Damjanovic, D. High-energy storage performance in $(Pb_{0.98}La_{0.02})(Zr_{0.45}Sn_{0.55})_{0.995}O_3$ AFE thick films fabricated via a rolling process. *J. Am. Ceram. Soc.* **99**, 3569-3572 (2016).
109. Liu, X., Li, Y. & Hao, X. Ultra-high energy-storage density and fast discharge speed of $(Pb_{0.98-x}La_{0.02}Sr_x)(Zr_{0.9}Sn_{0.1})_{0.995}O_3$ antiferroelectric ceramics prepared via the tape-casting method. *J. Mater. Chem. A* **7**, 11858-11866 (2019).
110. Ge, G. et al. Tunable domain switching features of incommensurate antiferroelectric ceramics realizing excellent energy storage properties. *Adv. Mater.* **34**, e2201333 (2022).
111. Guo, J. & Yang, T. Giant energy storage density in Ba, La co-doped $PbHfO_3$-based antiferroelectric ceramics by a rolling process. *J. Alloys Compd.* **888**, 161539 (2021).
112. Xu, R. et al. Investigation on antiferroelectricity of $Pb_{0.97}La_{0.02}(Hf_{1-x}Ti_x)O_3$ ceramics with low Ti content ($0 \le x \le 0.1$). *J. Am. Ceram. Soc.* **105**, 7438-7445 (2022).
113. Chao, W., Yang, T. & Li, Y. Achieving high energy efficiency and energy density in $PbHfO_3$-based antiferroelectric ceramics. *J. Mater. Chem. C* **8**, 17016-17024 (2020).
114. Xia, J. et al. Investigation on discharge behavior of antiferroelectric multilayer ceramic capacitors. *IEEE Trns. Dielectr. Electr. Insul.* **30**, 643-648 (2023).
115. Liu, X., Li, Y., Sun, N. & Hao, X. High energy-storage performance of PLZS antiferroelectric

multilayer ceramic capacitors. *Inorg. Chem. Front.* **7**, 756-764 (2020).

116. Liu, X., Zhao, Y., Sun, N., Li, Y. & Hao, X. Ultra-high energy density induced by diversified enhancement effects in $(Pb_{0.98-x}La_{0.02}Ca_x)(Zr_{0.7}Sn_{0.3})_{0.995}O_3$ antiferroelectric multilayer ceramic capacitors. *Chem. Eng. J.* **417**, 128032 (2021).
117. Wang, H., Zhao, P., Chen, L., Li, L. & Wang, X. Energy storage properties of $0.87BaTiO_3$-$0.13Bi[Zn_{2/3}(Nb_{0.85}Ta_{0.15})_{1/3}]O_3$ multilayer ceramic capacitors with thin dielectric layers. *J. Adv. Ceram.* **9**, 292-302 (2020).
118. Wang, H., Zhao, P., Chen, L. & Wang, X. Effects of dielectric thickness on energy storage properties of $0.87BaTiO_3$-$0.13Bi[Zn_{2/3}(Nb_{0.85}Ta_{0.15})_{1/3}]O_3$ multilayer ceramic capacitors. *J. Eur. Ceram. Soc.* **40**, 1902-1908 (2020).
119. Cai, Z. et al. High-temperature lead-free multilayer ceramic capacitors with ultrahigh energy density and efficiency fabricated via two-step sintering. *J. Mater. Chem. A* **7**, 14575-14582 (2019).
120. Zhao, P. et al. High-performance relaxor ferroelectric materials for energy storage applications. *Adv. Energy Mater.* **9**, 1803048 (2019).
121. Cai, Z. et al. Significantly enhanced dielectric breakdown strength and energy density of multilayer ceramic capacitors with high efficiency by electrodes structure design. *Appl. Phys. Lett.* **115**, 023901 (2019).
122. Li, W.-B. et al. $BaTiO_3$-based multilayers with outstanding energy storage performance for high temperature capacitor applications. *ACS Appl. Energy Mater.* **2**, 5499-5506 (2019).
123. Li, W.-B., Zhou, D., Xu, R., Pang, L.-X. & Reaney, I. M. $BaTiO_3$-$Bi(Li_{0.5}Ta_{0.5})O_3$, lead-free ceramics, and multilayers with high energy storage density and efficiency. *ACS Appl. Energy Mater.* **1**, 5016-5023 (2018).
124. Zhang, M. et al. Ultrahigh energy storage in high-entropy ceramic capacitors with polymorphic relaxor phase. *Science* **384**, 185-189 (2024).
125. Li, J. et al. Grain-orientation-engineered multilayer ceramic capacitors for energy storage applications. *Nat. Mater.* **19**, 999-1005 (2020).
126. Ji, H. et al. Ultrahigh energy density in short-range tilted nbt-based lead-free multilayer ceramic capacitors by nanodomain percolation. *Energy Storage Mater.* **38**, 113-120 (2021).
127. Ma, Z. et al. High-performance energy-storage ferroelectric multilayer ceramic capacitors via nano-micro engineering. *J. Mater. Chem. A* **11**, 7184-7192 (2023).

128. Li, J., Li, F., Xu, Z. & Zhang, S. Multilayer lead-free ceramic capacitors with ultrahigh energy density and efficiency. *Adv. Mater.* **30**, e1802155 (2018).

129. Tong, X.-Y. et al. Energy-storage properties of low-temperature Co-fired BNT-ST/AgPd multilayer lead-free ceramic capacitors. *J. Alloys Compd.* **827**, 154260 (2020).

130. Zhao, Y., Zhu, L., Meng, X., Li, Y. & Hao, X. Enhanced energy-storage properties in $Bi_{0.5}Na_{0.5}TiO_3$-$xSr_{0.85}Bi_{0.1}TiO_3$ by regulating relaxation temperature and constructing multilayer structure. *Mater. Sci. Eng. B* **282**, 115773 (2022).

131. Zhu, L.-F. et al. Boosting energy storage performance of $BiFeO_3$-based multilayer capacitors via enhancing ionic bonding and relaxor behavior. *J. Mater. Chem. A* **10**, 7382-7390 (2022).

132. Lu, Z. et al. Superior energy density through tailored dopant strategies in multilayer ceramic capacitors. *Energy Environ. Sci.* **13**, 2938-2948 (2020).

133. Wang, G. et al. Fatigue resistant lead-free multilayer ceramic capacitors with ultrahigh energy density. *J. Mater. Chem. A* **8**, 11414-11423 (2020).

134. Wang, G. et al. Ultrahigh energy storage density lead-free multilayers by controlled electrical homogeneity. *Energy Environ. Sci.* **12**, 582-588 (2019).

135. Wang, G. et al. Lead-free $(Ba,Sr)TiO_3$-$BiFeO_3$ based multilayer ceramic capacitors with high energy density. *J. Eur. Ceram. Soc.* **40**, 1779-1783 (2020).

136. Wang, D. et al. Bismuth ferrite-based lead-free ceramics and multilayers with high recoverable energy density. *J. Mater. Chem. A* **6**, 4133-4144 (2018).

137. Zhu, L.-F. et al. Composition and strain engineered $AgNbO_3$-based multilayer capacitors for ultra-high energy storage capacity. *J. Mater. Chem. A* **9**, 9655-9664 (2021).

138. Lv, Z. et al. $NaNbO_3$-based multilayer ceramic capacitors with ultrahigh energy storage performance. *Adv. Energy Mater.* **14**, 2304291 (2024).

139. Zhu, L.-F. et al. Energy-storage performance of $NaNbO_3$ based multilayered capacitors. *J. Mater. Chem. C* **9**, 7950-7957 (2021).